

Spitzer/IRS 5-35 μ m Low-Resolution Spectroscopy of the 12 μ m Seyfert Sample

Yanling Wu¹, Vassilis Charmandaris^{2,3}, Jiasheng Huang⁴, Luigi Spinoglio⁵, Silvia Tommasin^{5,6}

yanling@ipac.caltech.edu, vassilis@physics.uoc.gr, jhuang@cfa.harvard.edu, luigi.spinoglio@ifsi-roma.inaf.it, Silvia.Tommasin@ifsi-roma.inaf.it

ABSTRACT

We present low-resolution 5.5-35 μ m spectra for 103 galaxies from the 12 μ m Seyfert sample, a complete unbiased 12 μ m flux limited sample of local Seyfert galaxies selected from the *IRAS* Faint Source Catalog, obtained with the Infrared Spectrograph (IRS) on-board *Spitzer* Space Telescope. For 70 of the sources observed in the IRS mapping mode, uniformly extracted nuclear spectra are presented for the first time. We performed an analysis of the continuum emission, the strength of the Polycyclic Aromatic Hydrocarbon (PAH) and astronomical silicate features of the sources. We find that on average, the 15-30 μ m slope of the continuum is $\langle \alpha_{15-30} \rangle = -0.85 \pm 0.61$ for Seyfert 1s and -1.53 ± 0.84 for Seyfert 2s, and there is substantial scatter in each type. Moreover, nearly 32% of Seyfert 1s, and 9% of Seyfert 2s, display a peak in the mid-infrared spectrum at 20 μ m, which is attributed to an additional hot dust component. The PAH equivalent width decreases with increasing dust temperature, as indicated by the global infrared color of the host galaxies. However, no statistical difference in PAH equivalent width is detected between the two Seyfert types, 1 and 2, of the same bolometric luminosity. The silicate features at 9.7 and 18 μ m in Seyfert 1 galaxies are rather weak, while Seyfert 2s are more likely to display

¹Infrared Processing and Analysis Center, California Institute of Technology, 1200 E. California Blvd, MC 314-6, Pasadena, CA 91125

²University of Crete, Department of Physics, GR-71003, Heraklion, Greece

³IESL/Foundation for Research and Technology - Hellas, GR-71110, Heraklion, Greece, and Chercheur Associé, Observatoire de Paris, F-75014, Paris, France

⁴Harvard-Smithsonian Center for Astrophysics, 60 Garden Street, Cambridge, MA, 02138

⁵Istituto di Fisica dello Spazio Interplanetario, INAF, Via Fosso del Cavaliere 100, I-00133 Rome, Italy

⁶Dipartimento di Fisica, Università di Roma, La Sapienza, Roma, Italy

strong silicate absorption. Those Seyfert 2s with the highest silicate absorption also have high infrared luminosity and high absorption (hydrogen column density $N_H > 10^{23} \text{ cm}^{-2}$) as measured from the X-rays. Finally, we propose a new method to estimate the AGN contribution to the integrated $12 \mu\text{m}$ galaxy emission, by subtracting the "star formation" component in the Seyfert galaxies, making use of the tight correlation between PAH $11.2 \mu\text{m}$ luminosity and $12 \mu\text{m}$ luminosity for star forming galaxies.

1. Introduction

for which most of their nuclear and often bolometric luminosities is produced in

Active galaxies are galaxies in which one detects radiation from their nucleus which is due to accretion onto a super-massive black hole (SMBH) located at the center. The spectrum of an Active Galactic Nucleus (AGN) is typically flat in νf_ν . The fraction of the energy emitted from the AGN compared with the total bolometric emission of the host can range from a few percent in moderated luminosity systems ($L_{bol} < 10^{11} L_\odot$) to more than 90% in quasars ($L_{bol} > 10^{12} L_\odot$) (see Ho 2008, and references therein). As a subclass, Seyfert galaxies are the nearest and brightest AGNs, with 2-10keV X-ray luminosities less than $\sim 10^{44} \text{ ergs}^{-1}$ and their observed spectral line emission originates principally from highly ionized gas. Seyferts have been studied at many wavelengths, from X-rays, ultraviolet, optical, to infrared (IR) and radio. The analysis of their optical spectra has lead to the identification of two types, Seyfert 1s (Sy 1s) and Seyfert 2s (Sy 2s), with the type 1s displaying features of both broad ($\text{FWHM} > 2000 \text{ km s}^{-1}$) and narrow emission lines, while the type 2s only narrow-line emission.

The differences between the two Seyfert types have been an intense field of study for many years. Are they due to intrinsic differences in their physical properties, or are they simply a result of dust obscuration that hides the broad-line region in Sy 2s? A so-called unified model has been proposed (see Antonucci 1993; Urry & Padovani 1995), suggesting that Sy 1s and Sy 2s are essentially the same objects viewed at different angles. A dust torus surrounding the central engine blocks the optical light when viewed edge on (Sy 2s) and allows the nucleus to be seen when viewed face on (Sy 1s). Optical spectra in polarized light (Antonucci & Miller 1985) have indeed demonstrated for several Sy 2s the presence of broad lines, confirming for these objects the validity of the unified model. However, the exact nature of this orientation-dependent obscuration is not clear yet. Recently, more elaborate models, notably the ones of Elitzur (2008), Nenkova et al. (2008), and Thompson et al. (2009) suggest that the same observational constraints can also be explained with discrete

dense molecular clouds, without the need of a torus geometry.

The study of Seyfert galaxies is interesting also from a cosmological perspective, as they trace the build up of SMBHs at the centers of galaxies. Observations up to 10keV have established that the cosmic X-ray background (CXB) is mostly due to Seyferts with a peak in their redshift distribution at $z\sim 0.7$ (Hasinger et al. 2005). Furthermore, theoretical modeling of the observed number counts suggests that CXB at 30keV is also dominated by obscured Seyferts at $z\sim 0.7$ (Gilli et al. 2007; Worsley et al. 2005). Given the strong ionization field produced by the accretion disk surrounding a SMBH, the dust present can be heated to near sublimation temperatures, making an AGN appear very luminous in the mid-infrared (mid-IR).

Mid-IR spectroscopy is a powerful tool to examine the nature of the emission from AGNs, as well as the nuclear star-formation activity. Since IR observations are much less affected by dust extinction than those at shorter wavelengths, they have been instrumental in the study of obscured emission from optically thick regions in AGNs. This is crucial to understand the physical process of galaxy evolution. With the advent of the *Infrared Space Observatory (ISO)*, local Seyferts have been studied by several groups (see Verma et al. 2005, for a review). Mid-IR diagnostic diagrams to quantitatively disentangle the emission from AGNs, starbursts and quiescent star-forming (SF) regions have been proposed, using both spectroscopy and broad-band photometry (i.e. Genzel et al. 1998; Laurent et al. 2000). The recent launch of the *Spitzer* Space Telescope (Werner et al. 2004) has enabled the study of AGN with substantially better sensitivity and spatial resolution. In particular, using the Infrared Spectrograph (IRS¹) (Houck et al. 2004a) on board *Spitzer*, Weedman et al. (2005) demonstrated early into the mission the variety in the morphology displayed by the mid-IR spectra of eight classical AGNs. Since then, large samples of AGNs have been studied in detail, in an effort to quantify their mid-IR properties (Buchanan et al. 2006; Sturm et al. 2006; Deo et al. 2007; Gorjian et al. 2007; Hao et al. 2007; Tommasin et al. 2008). In addition, new mid-IR diagnostics have been developed to probe the physics of more complex sources, such as luminous and ultra luminous infrared galaxies (LIRGs/ULIRGs), which may also harbor AGNs. These were based on correlating the strength of the Polycyclic Aromatic Hydrocarbons (PAHs), high excitation fine-structure lines, as well as silicate features (i.e. Armus et al. 2007; Spoon et al. 2007; Charmandaris 2008; Nardini et al. 2008).

The extended 12 μm galaxy sample is a flux-limited (down to 0.22 Jy at 12 μm) sample of 893 galaxies selected from the IRAS Faint Source Catalog 2 (Rush et al. 1993). As dis-

¹The IRS was a collaborative venture between Cornell University and Ball Aerospace Corporation funded by NASA through the Jet Propulsion Laboratory and the Ames Research Center.

cussed by Spinoglio & Malkan (1989), all galaxies emit a nearly constant fraction ($\sim 7\%$) of their bolometric luminosity at $12\mu\text{m}$. As a result, selecting active galaxies based on their rest frame $12\mu\text{m}$ fluxes is the best approach to reduce selection bias due to the variations in their intrinsic spectral energy distributions (SED). A total of 116 objects from this sample have been optically classified as Seyfert galaxies (53 Sy 1s and 63 Sy 2s), providing one of the largest IR selected unbiased AGN sample. This sample also has ancillary data in virtually all wavelengths, thus making it the most complete data set for systematically studying the fundamental issues of AGNs in the infrared. Low-resolution $5.5\text{-}35\mu\text{m}$ Spitzer/IRS spectra of 51 Seyferts from the $12\mu\text{m}$ sample have been published by Buchanan et al. (2006), who focused on the study of the Seyfert types and the shape of mid-IR SED using principal component analysis. Based on this analysis and comparing with radio data, where available, they estimate the starburst contribution to the observed spectrum and find it to appear stronger in Sy 2s, in contrast to the unified model. However, high resolution *Spitzer* spectroscopy on 29 objects by Tommasin et al. (2008) does not find a clear indication of stronger star formation in Sy 2s than Sy 1s.

In this paper, we extend earlier work and study the mid-IR properties and nature of the dust enshrouded emission from 103 Seyferts of the $12\mu\text{m}$ Seyferts, nearly 90% of the whole sample. We use low resolution Spitzer/IRS spectra, focusing mainly on their broad emission and absorption features and provide for the first time our measurements of the PAH emission and strength of Si absorption features. Our observations and data reduction are presented in §2. In §3, we show our analysis on the mid-IR continuum shape, PAH emission and silicate strength of Seyfert galaxies. A new method to separate the star-formation and AGN contribution in the $12\mu\text{m}$ continuum is proposed in §4. Finally, we summarize our conclusions in §5.

2. Observations and Data Reduction

Since the launch of *Spitzer* in August 2003, a large fraction of the $12\mu\text{m}$ Seyfert galaxies have been observed by various programs using the low-resolution ($R\sim 64\text{-}128$) and high-resolution ($R\sim 600$) modules of Spitzer/IRS. These observations are publicly available in the *Spitzer* archive. A total of 84 galaxies have been observed with the low-resolution spectral mapping mode of the IRS by the GO program “Infrared SEDs of Seyfert Galaxies: Starbursts and the Nature of the Obscuring Medium” (PID: 3269), and mid-IR spectra extracted from the central regions of the maps for 51 galaxies were published by Buchanan et al. (2006). Spectra for the remaining sources have been taken as part of a number of Guaranteed, Open Time, as well as Legacy programs with program identifications (PID) 14, 61, 86, 96, 105, 159,

3237, 3624, 30291, and 30572. For the purpose of this work, which is mainly to use the PAH emission features to diagnose starburst and AGN contribution, we are focusing on the low-resolution IRS spectra (Short Low, SL: 5-15 μm ; Long Low, LL: 15-37 μm). We performed a complete search of the Spitzer Science Center (SSC) data archive and retrieved a total of 103 sources with at least Short Low observations. Among these objects, 47 are optically classified as Sy 1s and 56 as Sy 2s². We adopt the spectral classification of Rush et al. (1993) for the Seyfert types. Even though in a few cases, the classification may be ambiguous or may have changed, we do not expect our results, which are of statistical nature, to be affected. The complete list of the objects analyzed in this paper including their coordinates, IRAS fluxes, IR luminosity, redshift, Seyfert type and *Spitzer* program identification number are presented in Table 1. The redshift and luminosity distribution of the 12 μm Seyfert sample and the galaxies with IRS data studied in this paper is displayed in Figure 1.

With the exception of the data from the SINGS Legacy program (PID 159), of which we directly used spectra available at the SSC³, all other raw datasets are retrieved from the *Spitzer* archive and reduced in the following manner.

All except three⁴ of the 12 μm Seyferts with $cz < 10,000 \text{ km s}^{-1}$ have been observed with the IRS spectral mapping mode (PID 3269). This enabled us to also study the circumnuclear activity and examine the contribution of the host galaxy emission to the nuclear spectrum. Using datasets from this program, mid-IR spectra obtained from the central slit placement of each map with point-source extraction were published by Buchanan et al. (2006). However, as these authors have noted, since the observations had been designed as a spectral map, blind telescope pointing was used. As a result, no effort was made to accurately acquire each target and to ensure that the central slit of each map was indeed well centered on the source. Moreover, for sources where the mid-IR emission is extended, using a point-source extraction method would likely result in an overestimate of the flux densities, due to the slit loss correction function applied. This would consequently affect the SED of the galaxy.

For most of the data reduction in this paper, we used The CUbe Builder for IRS Spectra Maps (Smith et al. 2007b, CUBISM), in combination with an image convolution method. This method is developed explicitly for IRS mapping mode observations where the map

²The 12 μm Seyferts not included in this study due to lack of Spitzer/IRS SL spectra are 6 Sy 1s (Mrk1034, M-3-7-11, Mrk618, F05563-3820, F15091-2107, E141-G55) and 7 Sy 2s (F00198-7926, F00521-7054, E541-IG12, NGC1068, F03362-1642, E253-G3, F22017+0319).

³The SINGS data products are available at: <http://data.spitzer.caltech.edu/popular/sings/>. The nuclear spectra were extracted over a $50'' \times 33''$ region on the nucleus.

⁴The three exceptions are NGC1097, NGC1566, NGC5033, and they were also observed by SINGS.

size is small and involves the following steps. Spectral cubes were built using CUBISM from the IRS maps. Sky subtraction was performed by differencing the on and off source observations of the same order in each module (SL and LL). The observations from PID 3269 were designed to minimize redundancy and maximize the number of sources that can be observed using a limited amount of telescope time. As a result these maps consisted of only 13 steps in SL and 5 steps in LL with no repetition and for a source with extended mid-IR emission, the small map may not encompass the entire source, e.g. NGC1365. To obtain an accurate SED from the extracted region of the galaxy, one needs to ensure that the same fraction of source fluxes at all wavelengths is sampled. Since the point spread function (PSF) changes from 5 to 35 μm , we adopted an image convolution method to account for the change in the full width half maximum (FWHM) of the PSF: 2-dimensional images at each wavelength were convolved to the resolution at the longest wavelength (35 μm). Then low-resolution spectra were extracted with matched apertures, chosen to encompass the whole nuclear emission. Even though the image convolution method dilutes the fluxes included in the extraction aperture, it does ensure an accurate SED shape, especially for small maps that cannot encompass the extended emission for the source. A comparison of the LL spectra before and after image convolution for NGC1365 can be found in Figure 2.

A number of tests with varying sizes for the spectral extraction aperture were performed in order to select the optimum size. An aperture of 4×3 pixels in LL was adopted, which corresponds to an angular size of $20.4'' \times 15.3''$. Then a complete 5–35 μm spectrum of all galaxies centered on their nucleus was extracted⁵. The main motivation behind this choice was to ensure that we could produce an accurate overall SED of the extracted region, even in cases where the emission was extended. This was essential so that we have a reliable measurement of the continuum emission, in order to calculate the mid-IR slope, and to estimate the strength of the silicate features. Further tests were performed by extracting just the SL spectra of the sample using the smallest aperture possible (2×2 pixels in SL or $3.6'' \times 3.6''$). It was found that, in general, the measured fluxes and EWs of the PAH features did not differ more than 20% from the integrated spectra over the larger apertures, which indicates that these objects are likely to be less than 20% more extended than the point-spread-function of point sources. This suggests that most of the sources were not very extended in the mid-IR and more than 80% of their flux originates from a point source unresolved to Spitzer. Scaling the spectra between different orders and modules was not needed for most of the cases, and when an order mismatch was detected, the SL spectra were scaled to match LL. In Table 2, where we present our measurements, the sizes of the

⁵For two Sy 2s NGC1143/4 and NGC4922, only SL data were available, thus only 5–15 μm spectra were obtained.

extraction apertures as well as their corresponding projected linear sizes on the sky are also listed. A histogram of the physical size of extraction aperture for the whole sample is presented in Figure 3 with the dotted line, while in the same figure, we also show the distribution for sources that are observed in spectral mapping mode with the solid line. All the sources that are extracted from a projected size of more than 20 kpc are observed using the staring mode and reduced with point-source extraction method.

For data obtained with the IRS staring mode, the reduction was done in the following manner. We started from intermediate pipeline products, the “droop” files, which only lacked stray light removal and flat-field correction. Individual pointings to each nod position of the slit were co-added using median averaging. Then on and off source images were differenced to remove the contribution of the sky emission. Spectra from the final 2-D images were extracted with the Spectral Modeling, Analysis, and Reduction Tool (SMART, Higdon et al. 2004) in a point source extraction mode, which scaled the extraction aperture with wavelength to recover the same fraction of the diffraction limited instrumental PSF. Note that since the width of both the SL and LL slits is 2 pixels (3.6'' and 10.2'' respectively), no information could be retrieved along this direction from areas of the galaxy which were further away. The spectra were flux calibrated using the IRS standard star α Lac, for which accurate template was available (Cohen et al. 2003). Finally, using the first order of LL (LL1, 20–36 μ m) spectrum to define the absolute value of the continuum, the flux calibrated spectra of all other low-resolution orders were scaled to it.

For nine sources in the 12 μ m Seyfert sample, both spectral mapping and staring mode observations had been obtained and were available in the SSC data archive. For these galaxies, the spectra were extracted following the above mentioned recipes for all observations. In order to ascertain again how extended the emission from these source was, we compared the resulting spectra of the same source. With two exceptions, NGC4151 and NGC7213, all other seven spectra obtained in staring mode required a scaling factor larger than 1.15 between the SL and LL modules. This further suggests that the nuclear emission in those sources is indeed extended, and point-source extraction may not be appropriate. For galaxies with only staring mode observations, we also checked the difference between the overlap region ($\sim 15\mu$ m) in the SL and LL modules. None of them require a scaling factor more than 1.15, suggesting that those objects are point-like at least along the direction of the IRS slits.

3. Results

3.1. Global Mid-IR spectra of Seyfert Galaxies

It has been well established that the mid-IR spectra of Seyfert galaxies display a variety of features (see Clavel et al. 2000; Verma et al. 2005; Weedman et al. 2005; Buchanan et al. 2006; Hao et al. 2007, and references therein). This is understood since, despite the optical classification of their nuclear activity, emission from the circumnuclear region, as well as of the host galaxy, also influences the integrated mid-IR spectrum of the source. Our complete $12\ \mu\text{m}$ selected Seyfert sample provides an unbiased framework to study the statistics on their mid-IR properties. Earlier work by Buchanan et al. (2006) on just 51 AGN from this sample presented a grouping of them based on their continuum shapes and spectral features. In this section, we explore the global shape of the mid-IR spectra for the complete Spitzer/IRS set of data on the $12\ \mu\text{m}$ Seyferts.

We examine if the average mid-IR spectrum of a Sy 1 galaxy is systematically different from that of a Sy 2. The IRS spectra for 47 Sy 1s and 54 Sy 2s with full $5.5\text{--}35\ \mu\text{m}$ spectral coverage, normalized at the wavelength of $22\ \mu\text{m}$, are averaged and plotted in Figure 4. For comparison, we over-plot the average starburst template from Brandl et al. (2006). It is clear that the mid-IR continuum slope of the average Sy 1 spectrum is shallower than that of Sy 2, while the starburst template has the steepest spectral slope, indicating a different mixture of hot/cold dust component in these galaxies (also see Hao et al. 2007). This would be consistent with the interpretation that our mid-IR spectra of Sy 2s display a strong starburst contribution, possibly due to circumnuclear star formation activity included in the aperture we used to extract the spectra from, consistent with the findings of Buchanan et al. (2006) that star formation is extended and it is not a purely nuclear phenomenon. PAH emission, which is a good tracer of star formation activity (Förster Schreiber et al. 2004), can be detected in the average spectra of both Seyfert types, while it is most prominent in the average starburst spectrum. PAH emission originates from photo-dissociation region (PDR) and can easily be destroyed by the UV/X-ray photons in strong a radiation field produced near massive stars and/or an accretion disk surrounding a SMBH (Voit 1992; Laurent et al. 2000; Clavel et al. 2000; Sturm et al. 2002; Verma et al. 2005; Weedman et al. 2005). In the $12\ \mu\text{m}$ Seyfert sample, we detect PAH emission in 37 Sy 1s and 53 Sy 2s, that is 78% and 93% for each type respectively. This is expected since the apertures we used to extract the mid-IR spectra for the $12\ \mu\text{m}$ sample correspond in most cases to areas of more than 1 kpc in linear dimensions (see Figure 3). As a result, emission from the PDRs associated with the extended circumnuclear region and the disk of the host galaxy is also encompassed within the observed spectrum. High ionization fine-structure lines, such as $[\text{NeV}]14.32\ \mu\text{m}/24.32\ \mu\text{m}$, are clearly detected even in the low-resolution average spectrum of Sy 1. This signature

is also visible, though rather weak, in the average spectrum of Sy 2, while it is absent in the average starburst template. Due to photons of excitation energy higher than 97eV and typically originating from the accretion disk of an AGN, [NeV] serves as an unambiguous indicator of an AGN. Even though the low-resolution module of IRS was not designed for studying fine-structure lines, we are still able to detect [NeV] emission in 29 Sy 1s and 32 Sy 2s, roughly 60% for both types. Another high ionization line, [OIV] 25.89 μm , with ionization potential of 54eV, also appears in both Seyfert types (42 Sy 1s and 41 Sy 2s), and is stronger in the average spectrum of Sy 1. The [OIV] emission line can be powered by shocks in intense star forming regions or AGNs (see Lutz et al. 1998; Schaerer & Stasińska 1999; Bernard-Salas et al. 2009; Hao et al. 2009). In our sample it is probably powered by both, given the large aperture we adopted for spectral extraction. More details and a complete analysis of mid-IR fine-structure lines for 29 galaxies from the 12 μm Seyfert sample are presented in Tommasin et al. (2008), while the work for the entire sample is in progress (Tommasin et al. 2009).

An atlas with mid-IR low-resolution spectra of the 12 μm Seyfert sample is included at the end of this paper⁶. We find that a fraction of our sources show a flattening or a local maximum in the mid-IR continuum at $\sim 20 \mu\text{m}$, which had also been noted as a “broken power-law” in some Seyfert galaxies by Buchanan et al. (2006). Another more extreme such case was the metal-poor blue compact dwarf galaxy SBS0335-052E (Houck et al. 2004b), and it was interpreted with the possible absence of larger cooler dust grains in the galaxy. Since the change of continuum slope appears at $\sim 20 \mu\text{m}$, we use the flux ratio at 20 and 30 μm , F_{20}/F_{30} , to identify these objects. After further examination of the spectra, we find 15 Sy 1s and 4 Sy 2s, which have a $F_{20}/F_{30} \geq 0.95$. We call these objects “20 μm peakers”.

To analyse the properties of “20 μm peakers”, we plot the average IRS spectra of the 19 sources in Figure 5. As most of these sources are type 1 Seyferts (15 out of 19), we also overplot the average Sy 1 spectrum for comparison. In addition to their characteristic continuum shape, a number of other differences between the “20 μm peakers” and Sy 1s are also evident. PAH emission, which is clearly detected in the average Sy 1 spectrum, appears to be rather weak in the average “20 μm peaker” spectrum. The high-ionization lines of [NeV] and [OIV] are seen in both spectra with similar strength, while low-ionization lines, especially [NeII] and [SIII], are much weaker in the average spectrum of “20 μm peakers”. If we calculate the infrared color of a galaxy using the ratio of F_{25}/F_{60} (see section 3.3 for more detailed discussion on this issue), we find an average value of 0.75 for the “20 μm peakers”, while it is 0.30 for the other “non-20 μm peaker” Sy 1s in the 12 μm sample. Finally, the

⁶All spectra are also available in electronic format.

average IR luminosities of the “20 μm peakers” and Sy 1s do not show significant difference, with $\log(L_{\text{IR}}/L_{\odot})=10.96$ for the former and $\log(L_{\text{IR}}/L_{\odot})=10.86$ for the latter. These results are consistent with the “20 μm peakers” being AGNs with a dominant hot dust emission from a small grain population heated to effective temperatures of $\sim 150\text{K}$ and a possible contribution due to the distinct emissivity of astronomical silicates at $18\mu\text{m}$. Their radiation field must also be stronger than a typical Sy 1, since it destroys the PAH molecules around the nuclear region more efficiently. We should stress that unlike SBS0335-052E, whose global IR SED peaks at $\sim 30\mu\text{m}$, and likely has limited quantities of cold dust, the mid-IR peak we observe in these objects at $\sim 20\mu\text{m}$ is likely a local one⁷. This becomes more evident in Figure 6, where we also include the scaled average 60 and 100 μm flux densities for the “20 μm peakers”. It is clear that their far-IR emission increases with wavelength, thus confirming the presence of ample quantities cold dust in these objects. To contrast the global SED of these objects with the whole Seyfert sample we include in Figures 7 and 8 the average SED of the Sy 1s and Sy 2s of the sample. All SEDs have been normalized as in Figure 4 at $22\mu\text{m}$. Unlike the “20 μm peakers” one can easily observe the regular increase of the flux from ~ 15 to $60\mu\text{m}$ in the average Sy 1 and Sy 2 SEDs. A more detailed analysis of the dust properties of the “20 μm peakers” in comparison with typical active galaxies will be presented in a future paper.

3.2. The PAH emission in the $12\mu\text{m}$ Seyferts

In this section, we explore some of the properties of the PAH emission in our sample and contrast our findings to the previous work. To quantify the strength of PAH emission, we follow the usual approach and measure the fluxes and equivalent widths (EWs) of the 6.2 and $11.2\mu\text{m}$ PAH features from their mid-IR spectra. Even though the $7.7\mu\text{m}$ PAH is the strongest of all PAHs (Smith et al. 2007a), we prefer not to include it in our analysis. This is due to the fact that its measurement is affected by absorption and emission features next to it and depends strongly both on the assumptions of the various measurement methods (spline or Drude profile fitting) as well as the underlying continuum. Furthermore, it often spans between the two SL orders, which could also affect its flux estimate. The 6.2 and $11.2\mu\text{m}$ PAH EWs are derived by integrating the flux of the features above an adopted continuum and then divide by the continuum fluxes in the integration range. The baseline is determined by fitting a spline function to the selected points ($5.95\text{-}6.55\mu\text{m}$ for the $6.2\mu\text{m}$ PAH and $10.80\text{-}11.80\mu\text{m}$ for the $11.2\mu\text{m}$ PAH). The PAH EWs as well as the integrated fluxes are listed in Table 2. The errors including both flux calibration and measurement are

⁷However, some objects, such as Mrk335, Mrk704 and 3C234, do have IRAS ratios of $F_{25}/F_{60} > 1$.

estimated to be less than $\sim 15\%$ on average.

The first study on the PAH properties of a large sample of Seyferts was presented by Clavel et al. (2000), using ISO/PHOT-S 2.5–11 μm spectra and ISO/CAM broad band mid-IR imaging. The authors suggested that there was a statistical difference in the strength of the PAH emission and the underlying hot continuum ($\sim 7\mu\text{m}$) emission between type 1 and type 2 objects. They also found that Sy 2s had stronger PAHs than Sy 1s, while Sy 1s had higher hot continuum associated with emission from the AGN torus. This was consistent with an orientation depended depression of the continuum in Sy 2s. The interpretation of these results was challenged by Lutz et al. (2004), who attributed it to the large ($24'' \times 24''$) aperture of ISO/PHOT-S, and the possible contamination from the host galaxy. More recently, Deo et al. (2007) have found a relation between the 6.2 μm PAH EWs and the 20-30 μm spectral index⁸, with a steeper spectral slope seen in galaxies with a stronger starburst contribution. This is understood since galaxies hosting an AGN are “warmer” and have an IR SED peaking at shorter wavelengths thus appearing flatter in the mid-IR (see also next section). Given the global correlations between star formation activity and PAH strength (Förster Schreiber et al. 2004; Peeters et al. 2004; Wu et al. 2005; Calzetti et al. 2005, 2007, i.e.), star-forming galaxies are expected to also have stronger PAH features. In Figure 9, we plot the 15-30 μm ⁹ spectral index for the 12 μm Seyfert sample as a function of their 11.2 μm PAH EWs. The diamonds indicate the starburst galaxies from Brandl et al. (2006)¹⁰. A general trend of the PAH EWs decreasing as a function of 15-30 μm spectral index is observed in Figure 9, even though it is much weaker than the anti-correlation presented by Deo et al. (2007). Starburst galaxies are located on the upper left corner of the plot, having very steep spectral slopes, with $\langle \alpha_{15-30} \rangle = -3.02 \pm 0.50$, and large PAH EWs, nearly 0.7 μm . Seyfert galaxies spread over a considerably larger range in spectral slopes as well as PAH EWs. Sy 1s and Sy 2s are mixed on the plot. On average, the 15-30 μm spectral index is $\langle \alpha_{15-30} \rangle = -0.85 \pm 0.61$ for Sy 1s and $\langle \alpha_{15-30} \rangle = -1.53 \pm 0.84$ for Sy 2s. Note that although the mean spectral slope is slightly steeper for Sy 2s, there is substantial scatter, as is evident by the uncertainties of the mean for each types (see also Figure 7 and 8).

It is well known that the flux ratio of different PAH emission bands is a strong function of PAH size and their ionization state (Draine & Li 2001). The 6.2 μm PAH emission is due

⁸The spectral index α is defined as $\log(F1/F2)/\log(\nu1/\nu2)$.

⁹We choose to use α_{15-30} so that we can directly make use of the spectral index measurement for the starburst galaxies in the Brandl et al. (2006) sample.

¹⁰We have excluded the 6 galaxies that have AGN signatures from the Brandl et al. (2006) starburst sample.

to C-C stretching mode and the $11.2\ \mu\text{m}$ feature is produced by C-H out-of-plane bending mode (Draine 2003). In Figure 10, we display a histogram of the $11.2\ \mu\text{m}$ to $6.2\ \mu\text{m}$ PAH flux ratios for the $12\ \mu\text{m}$ Seyferts. Given the relatively small number of starburst galaxies in the Brandl et al. (2006) sample (16 sources), we also included 20 HII galaxies from the SINGS sample of Smith et al. (2007a), thus increasing the number of SF galaxies to 36 sources and making its comparison with the Seyferts more statistically meaningful. However, since Smith et al. (2007a) adopted multiple Drude profile fitting for the measurement of PAH features, for reasons of consistency, we re-measured the PAH fluxes of the 20 SINGS galaxies with our spline fitting method. From Figure 10, we can see that both the Seyferts and SF galaxies, indicated by the solid and dashed line respectively, appear to have very similar distribution of PAH $11.2\ \mu\text{m}/6.2\ \mu\text{m}$ band ratios. The average PAH flux ratios for the Seyfert sample is 0.94 ± 0.37 while for the SF galaxies is 0.87 ± 0.24 , which agree within $1\text{-}\sigma$. This is also consistent with the findings of Shi et al. (2007), who reported similar $11.2\ \mu\text{m}/7.7\ \mu\text{m}$ flux ratios between a sample of higher redshift AGNs (PG, 2MASS and 3CR objects) and the SINGS HII galaxies. This implies that even though the harsh radiation field in AGNs may destroy a substantial amount of the circumnuclear PAH molecules, and does so preferentially – the smaller PAHs being destroyed first (Draine & Li 2001; Smith et al. 2007a) – it likely does not do so over a large volume. Enough molecules in the circumnuclear regions do remain intact and as a result, the aromatic features that we observe from Seyferts are essentially identical to those in SF galaxies.

The relative strength of PAH emission can also be used to examine the validity of the unified AGN model. As mentioned earlier, this model attributes the variation in AGN types as the result of dust obscuration and relative orientation of the line of sight to the nucleus (Antonucci 1993). Sy 1s and Sy 2s are intrinsically the same but appear to be different in the optical, mainly because of the much larger extinction towards the nuclear continuum of Sy 2s when viewed edge on. The latest analysis of the IRS high-resolution spectra of 87 galaxies from the $12\ \mu\text{m}$ Seyfert sample shows that the average $11.2\ \mu\text{m}$ PAH EW is $0.29\pm 0.38\ \mu\text{m}$ for Sy 1s and $0.37\pm 0.35\ \mu\text{m}$ for Sy 2s (Tommasin et al. 2009, in preparation). As we show in Table 3, the $11.2\ \mu\text{m}$ PAH EWs of the whole $12\ \mu\text{m}$ Seyfert sample (90 objects excluding upper limits) is $0.21\pm 0.22\ \mu\text{m}$ for the Sy 1s and $0.38\pm 0.30\ \mu\text{m}$ for the Sy 2s. The difference we observe in the PAH EWs between the two Seyfert types is somewhat larger than the one reported by Tommasin et al. (2009, in preparation), though still consistent within 1σ . This further suggests that there is little discernible difference between Sy 1s and Sy 2s at this wavelength.

If the observed AGN emission in the infrared does not depend on the line of sight of the observer, one can compare the circumnuclear PAH emission of Sy 1s and Sy 2s of similar bolometric luminosities to test the unified model. If we bin the sources according to their

IR luminosity, we find an average PAH EW of $0.22 \pm 0.23 \mu\text{m}$ for Sy 1s and $0.40 \pm 0.30 \mu\text{m}$ for Sy 2s with $L_{\text{IR}} < 10^{11} L_{\odot}$; while the average PAH EWs are $0.19 \pm 0.19 \mu\text{m}$ for Sy 1s and $0.37 \pm 0.30 \mu\text{m}$ for Sy 2s with $L_{\text{IR}} \geq 10^{11} L_{\odot}$ (see Table 3 for a summary of these results). The difference between the two Seyfert types is still less than 1σ . This result is not in agreement with the findings of Buchanan et al. (2006) who based on a principle component analysis find that in their subset of 51 galaxies the Sy 2s show a stronger starburst eigenvector/template contribution than the Sy 1s. As the authors suggest this might be due to a bias of selection effects. Our result can be interpreted as indicating that there is some, but not substantial obscuration in the mid-IR. As a consequence we are able to probe deep into the nuclear region, sampling most of the volume responsible for the mid-IR emission. This result is consistent with a similar finding of Buchanan et al. (2006) who compared the mid-IR to radio ratio for their sample. They concluded that the observed factor of ~ 2 difference between the two types would imply either a smooth torus which is optically thin in the mid-IR or a clumpy one containing a steep radial distribution of optically thick dense clumps (Nenkova et al. 2008).

3.3. Cold/Warm AGN diagnostics

The *IRAS* 25 and 60 μm flux ratio has long been used to define the infrared color (“warm” or “cold”) of a galaxy, with “warm” galaxies having a ratio of $F_{25}/F_{60} > 0.2$ (Sanders et al. 1988). In Figure 11, we plot the 11.2 μm PAH EW as a function of the flux ratio between F_{25} and F_{60} for the 12 μm Seyfert sample. The *IRAS* 25 and 60 μm fluxes were compiled from Rush et al. (1993) and Sanders et al. (2003) and are listed in Table 1. The aperture of the *IRAS* broad band filters is on the order of a few arcminutes on the sky¹¹ and typically encompass the whole galaxy, while the PAH EW is measured from a spectrum of a smaller region centered on the nucleus of the galaxy (see Table 2). Nevertheless, we observe a clear trend of the 11.2 μm PAH EW decreasing with F_{25}/F_{60} ratio in Figure 11. On this plot, we also include the SF galaxies from Brandl et al. (2006) and Smith et al. (2007a). All SF galaxies appear to be clustered on the top left corner of the plot, having high PAH EWs and low F_{25}/F_{60} values, suggesting strong star formation and cooler dust temperatures. The observed suppression of PAH emission seen in the warm AGNs implies that the soft X-ray and UV radiation of the accretion disk, which destroys the PAH molecules, is also reprocessed by the dust and dominates the mid- and far-IR colors. More specifically,

¹¹According to the *IRAS* Explanatory Supplement Document for unenhanced coadded *IRAS* images the resolution is approximately $1' \times 5'$, $1' \times 5'$, $2' \times 5'$ and $4' \times 5'$ at 12, 25, 60 and 100 μm , respectively (see <http://lambda.gsfc.nasa.gov/product/iras/docs/exp.sup>).

warm Sy 1s have an average $11.2\mu\text{m}$ PAH EW of $0.10\pm 0.12\mu\text{m}$, while for Sy 2s the value is $0.18\pm 0.24\mu\text{m}$. Similarly for the cold sources, the average PAH EW is $0.40\pm 0.23\mu\text{m}$ for Sy 1s and $0.59\pm 0.19\mu\text{m}$ for Sy 2s. We observe a $\sim 3\sigma$ difference in the PAH EWs between the cold and warm sources, independent of their Seyfert type. This indicates that as the emission from the accretion disk surrounding the SMBH of the active nucleus contributes progressively more to the IR luminosity, its radiation field also destroys more of the PAH molecules and thus diminishes their mid-IR emission.

The trend of PAH EWs decreasing with F_{25}/F_{60} has also been detected in a large sample of ULIRGs studied by Desai et al. (2007). The luminosities of the $12\mu\text{m}$ Seyfert sample are more comparable with LIRGs, thus our work extends the correlation of Desai et al. (2007) to a lower luminosity range. This is rather interesting since deep photometric surveys with *Spitzer* can now probe normal galaxies as well as LIRGs at $z\sim 1$ (Le Floc'h et al. 2005), a fraction of which are known to host an AGN based on optical spectra and mid-IR colors (Fadda et al. 2002; Stern et al. 2005; Brand et al. 2006).

We have also investigated the dependence of the $6.2\mu\text{m}$ PAH EW on the F_{25}/F_{60} ratio for our sample. A similar trend of the $6.2\mu\text{m}$ EWs decreasing with F_{25}/F_{60} is observed as well, though there is larger scatter than the one seen with the $11.2\mu\text{m}$ feature. This is probably due to the fact that the $6.2\mu\text{m}$ PAH EW is intrinsically fainter and only upper limits could be measured for a number of source (see Table 2). Despite the scatter, this trend is still a rather important finding, because for high redshift galaxies ($z>2.5$), the 6.2 and $7.7\mu\text{m}$ PAHs might be the only features available in the wavelength range covered by the IRS, thus measuring them can reveal essential information on the star-formation luminosity and dust composition of high-redshift galaxies (see Houck et al. 2005; Yan et al. 2005; Teplitz et al. 2007; Weedman & Houck 2008).

3.4. The Silicate Strength of the $12\mu\text{m}$ Seyferts

In the mid-IR regime, one can examine not only the structure of complex organic molecules and determine their aromatic or aliphatic nature, but can also probe the chemistry of dust grains (see van Dishoeck 2004). One of the most prominent continuum features in the $5\text{-}35\mu\text{m}$ range is the one associated with the presence of astronomical silicates in the grains, which are characterized by two peaks in the emissivity at 9.7 and $18\mu\text{m}$ (see Dudley & Wynn-Williams 1997). The silicate features had been detected in absorption in SF galaxies, protostars and AGN for over 30 years (ie Gillett et al. 1975; Rieke & Low 1975), but it was the advent of space observatories such as *ISO* and *Spitzer*, which allowed for the first time of study over a wide range of astronomical objects and physical conditions. According

to the unified model, an edge-on view through the cool dust in the torus will cause the silicate feature to be seen in absorption, while with a face-on view, the hot dust at the inner surface of the torus will cause an emission feature for the silicate (Efstathiou & Rowan-Robinson 1995). Even though silicate in emission at $9.7\mu\text{m}$ had already been observed in the SF region N66 (Contursi et al. 2000), emission at both $9.7\mu\text{m}$ and $18\mu\text{m}$ in AGNs and Quasars was detected with *Spitzer* (Siebenmorgen et al. 2005; Hao et al. 2005; Sturm et al. 2005), providing strong support for the unified model (Antonucci 1993). Using *Spitzer*/IRS data, Hao et al. (2007) compiled a large, though inhomogeneous sample of AGNs and ULIRGs, and uniformly studied the silicate features in these galaxies. Using the same sample, Spoon et al. (2007) proposed a new diagnostic of mid-IR galaxy classification based on the strength of silicate and PAH features. To put in the same context the properties of the silicate feature in the $12\mu\text{m}$ Seyfert sample, we also measured the strength of the silicate at $9.7\mu\text{m}$, using the definition and approach of Spoon et al. (2007) as:

$$S_{\text{sil}} = \ln \frac{f_{\text{obs}}(9.7\mu\text{m})}{f_{\text{cont}}(9.7\mu\text{m})} \quad (1)$$

where $f_{\text{cont}}(9.7\mu\text{m})$ is the flux density of a local mid-IR continuum, defined from the 5-35 μm IRS spectrum. Sources with silicate in emission have positive strength and those in absorption negative. Buchanan et al. (2006) did identify two AGN with silicate emission and two more with broad silicate absorption out of the 51 sources they studied. In this paper, we provide for the first time measurements on the silicate features for this complete sample. We follow the prescription of Spoon et al. (2007) and Sirocky et al. (2008) for the continuum definition and identify the sources to be PAH-dominated, continuum-dominated and absorption-dominated. The values of S_{sil} measured from the $12\mu\text{m}$ Seyferts can be found in Table 2.

In Figure 12a, we plot the $11.2\mu\text{m}$ PAH EWs as a function of the $9.7\mu\text{m}$ silicate strength¹². We observe that most Sy 1s are located close to $S_{\text{sil}}=0$ and the range of their silicate strength is rather narrow, with the exception of one galaxy, UGC5101, which is also one of the ULIRGs of the Bright Galaxy Sample (Armus et al. 2004, 2007). This is in agreement with the results of Hao et al. (2007), who found that Sy 1s are equally likely to display the $9.7\mu\text{m}$ silicates feature in emission and in absorption. The Sy 2s have a larger scatter in the value of the silicate strength, with most of them showing the feature in absorption. The

¹²A similar plot using the $6.2\mu\text{m}$ PAH EWs was proposed by Spoon et al. (2007) as a mid-IR galaxy classification method

average silicate strength of the $12\ \mu\text{m}$ Seyfert sample is -0.07 ± 0.29 for Sy 1s and -0.46 ± 0.73 for Sy 2s, while the median values are -0.02 for Sy 1s and -0.23 for Sy 2s. Overall, though selected at $12\ \mu\text{m}$, most objects have a rather weak silicate strength, with only 18 Sy 2s and 2 Sy1s displaying values of $S_{\text{sil}} < -0.5$. We also examined the dependence of the silicate strength with the IR luminosity of the objects and plot it in Figure 12b. Except for one galaxy (NGC7172), all the sources with deep silicate absorption features have IR luminosities larger than $10^{12}L_{\odot}$, and thus are also classified as ULIRGs. In Sy 1 galaxies, even when their luminosities are larger than $10^{12}L_{\odot}$, the $9.7\ \mu\text{m}$ silicate strength is still near zero, while high-luminosity Sy 2s are more likely to have deep silicate absorption features.

We also compare the silicate strength with galaxy color, as defined in §3.3. In Figure 13a, we plot the silicate strength as a function of the IRAS flux ratio of F25/F60. Since the majority of the galaxies do not have strong silicate features, no clear correlation between the two parameters is seen. We notice that galaxies with $S_{\text{sil}} < -1$ also appear to have colder colors. This indicates that more dust absorption is present in sources with the colder IR SEDs, even though many sources with small F25/F60 ratios do not display any silicate absorption features.

Finally, we investigate the relation between the mid-IR silicate strength and the hydrogen column density¹³, as measured from the X-rays. The latter can measure directly the absorption in active galaxies: the power law spectrum in the 2-10keV range may be affected by a cutoff due to photo-electric absorption, from which column densities of $10^{22} - 10^{24}\text{cm}^{-2}$ are derived (eg. Maiolino et al. 1998). One should note though that due to the substantially smaller physical size of the nuclear region emitting in (hard) X-rays this measurement is more affected by the clumpiness of the intervening absorbing medium. The well established observational fact that Sy 2s are preferentially more obscured than Sy 1s, as has been shown both in the optical and in the X-ray spectra, is also apparent in the mid-IR spectra by our results given in Figure 13b. We find that sources with weak silicate absorption or emission features span over all values of the column densities. However, most of the sources with a strong silicate absorption ($S_{\text{sil}} < -0.5$) have a $N_H > 10^{23}\text{ (cm}^{-2}\text{)}$ (11 of 15 sources), and Sy 2s dominate this group (13 of 15 sources).

¹³The values of the hydrogen column density have been taken from Markwardt et al. (2005); Bassani et al. (2006); Sazonov et al. (2007); Shu et al. (2007).

4. What powers the $12\ \mu\text{m}$ luminosity in the $12\ \mu\text{m}$ Seyferts?

The use of the global infrared dust emission as a tracer of the absorbed starlight and associated star formation rate has been known since the first results of IRAS (see Kennicutt 1998 and references there in). At $12\ \mu\text{m}$, the flux obtained from the *IRAS* broadband filter is dominated by the continuum emission, though it could also be affected by several other discrete factors, including the silicate features, the PAH emission, fine-structure lines, etc. In Figure 14, we present the usual plot of $L_{12\ \mu\text{m}}/L_{\text{IR}}$ versus the total IR luminosity¹⁴ for the Seyfert galaxies and SF galaxies. A clear correlation between these two parameters, originally presented for the $12\ \mu\text{m}$ sample by Spinoglio et al. (1995), is seen. The two Seyfert types do not show significant differences. SF galaxies appear to have a lower fractional $12\ \mu\text{m}$ luminosity when compared to Seyferts of similar total IR luminosity. This can be explained by the presence of hot dust emission ($T > 300\text{K}$) originating from regions near the active nucleus, contributing more strongly at the shortest wavelengths (5 to $15\ \mu\text{m}$) of the IR SED. This is consistent with the results of Spinoglio et al. (1995), who have shown that the $12\ \mu\text{m}$ luminosity is $\sim 15\%$ of the bolometric luminosity¹⁵ in AGNs (Spinoglio & Malkan 1989), while only $\sim 7\%$ in starburst and normal galaxies.

Following these early IRAS results, a number of studies have explored the issue of distinguishing AGN from the star formation signatures in the mid-IR and to determine the fractional contribution of each component to the IR luminosity for local (i.e. Genzel et al. 1998; Laurent et al. 2000; Peeters et al. 2004; Buchanan et al. 2006; Farrah et al. 2007; Nardini et al. 2008) and high redshift sources (i.e. Brand et al. 2006; Weedman et al. 2006; Sajina et al. 2007). More recently, using the [OIV] $25.89\ \mu\text{m}$ line emission as an extinction free tracer of the AGN power, Meléndez et al. (2008b) were able to decompose the stellar and AGN contribution to the [NeII] $12.81\ \mu\text{m}$ line. These authors have compiled a sample from existing *Spitzer* observations by Deo et al. (2007); Tommasin et al. (2008); Sturm et al. (2002); Weedman et al. (2005), as well as X-ray selected sources from Meléndez et al. (2008a). They found that Sy 1 and Sy 2 galaxies are different in terms of the relative AGN/starburst contribution to the infrared emission, with star formation being responsible for $\sim 25\%$ of the mid- and far-IR continuum in Sy 1s, and nearly half of what was estimated for Sy 2s.

In Figure 15a and 15b, we plot $L_{11.2\ \mu\text{mPAH}}/L_{\text{FIR}}$ and $L_{11.2\ \mu\text{mPAH}}/L_{\text{IR}}$ as a function of the

¹⁴Calculated from the *IRAS* flux densities following the prescription of Sanders & Mirabel (1996): $L_{\text{IR}} = 5.6 \times 10^5 D_{\text{Mpc}}^2 (13.48 S_{12} + 5.16 S_{25} + 2.58 S_{60} + S_{100})$.

¹⁵According to Spinoglio et al. (1995), the bolometric luminosity is derived by combining the blue photometry, the near-IR and FIR luminosities, as well as an estimate of the flux contribution from cold dust longward of $100\ \mu\text{m}$.

far-infrared (FIR) luminosity¹⁶ and the total IR luminosity for the Seyferts and SF galaxies. For both the SF galaxies and the Seyferts, their PAH luminosity appear to have a nearly constant fraction of their FIR luminosity, which would be expected since both quantities have been used as indicators of the star-formation rate. However, for a given PAH luminosity, Seyfert galaxies display an excess in the total IR luminosity compared to starburst systems. This is also understood as the total IR luminosity is the sum of mid-IR and FIR luminosity and consequently it is affected by the AGN emission in the mid-IR. We propose a simple method to the mid-IR excess and estimate the AGN contribution to the 12 μm luminosity.

In Figure 16, we plot the $L_{11.2\mu\text{mPAH}}/L_{12\mu\text{m}}$ versus the 12 μm luminosity for the Seyfert and SF galaxies. There is a clear correlation for SF galaxies with an average $L(11.2\mu\text{m PAH})/L(12\mu\text{m})$ ratio of 0.044 ± 0.010 . Since there is no AGN contamination in the 12 μm luminosity for these galaxies, we can attribute all mid-IR continuum emission to star formation. Seyfert galaxies display a larger scatter on this plot, and we decompose their 12 μm luminosity into two parts: one contributed by the star formation activity, which is proportional to their PAH luminosity, and one due to dust heated by the AGN. If we assume that the star formation component in the 12 μm luminosity of Seyferts is associated with the 11.2 μm PAH luminosity in the same manner as in SF galaxies, then we can estimate the star formation contribution to the integrated 12 μm luminosity of the Seyfert sample. Subtracting this SF contribution from the total 12 μm luminosity, we can obtain, in a statistical sense, the corresponding AGN contribution.

To check the validity of this method, we plot in Figure 17 the “AGN fraction” as a function of the IRAC 8 μm to *IRAS* 12 μm flux ratios. We define “AGN fraction” as the AGN luminosity estimated using the above method divided by the total 12 μm luminosity: $\text{AGN fraction}(12\mu\text{m}) = (L_{12\mu\text{m}} - L_{\text{SF}})/L_{12\mu\text{m}}$. The IRAC 8 μm flux will be dominated by PAH emission when PAHs are present, thus normalizing by the 12 μm flux provides an estimate of the PAH EW¹⁷. As one would expect, examining the Seyferts for which an AGN fraction was not a lower limit, an anti-correlation between the two parameters is visible. This suggests that our method of decomposing the 12 μm luminosity is reasonable. Since the scatter in the linear fit for SF galaxies in Figure 16 is $\sim 25\%$, this translates directly to the “AGN fraction” we have obtained. We estimate the uncertainty of our calculated “AGN fraction” to be no better than $\sim 25\%$.

¹⁶Calculated from the *IRAS* flux densities following the prescription of Sanders & Mirabel (1996): $L_{\text{FIR}} = 5.6 \times 10^5 D_{\text{Mpc}}^2 (2.58 S_{60} + S_{100})$

¹⁷A similar approach using Spitzer broad band filters was used successfully by Engelbracht et al. (2008) to estimate the PAH contribution in starburst galaxies.

5. Conclusions

We have analyzed Spitzer/IRS data for a complete unbiased sample of Seyfert galaxies selected from the *IRAS* Faint Source Catalog based on their $12\mu\text{m}$ fluxes. We extended earlier work on the same sample by Buchanan et al. (2006) who have published spectra for 51 objects and explored the continuum shapes and the differences between Seyfert types. In our study, we present 5– $35\mu\text{m}$ low-resolution spectra for 103 objects, nearly 90% of the whole $12\mu\text{m}$ Seyfert sample. The main results of our study are:

1. The $12\mu\text{m}$ Seyferts display a variety of mid-IR spectral shapes. The mid-IR continuum slopes of Sy 1s and Sy 2s are on average $\langle \alpha_{15-30} \rangle = -0.85 \pm 0.61$ and -1.53 ± 0.84 respectively, though there is substantial scatter for both types. We identify a group of objects with a local maximum in their mid-IR continuum at $\sim 20\mu\text{m}$, which is likely due to the presence of a warm $\sim 150\text{K}$ dust component and $18\mu\text{m}$ emission from astronomical silicates. Emission lines, such as the [NeV] $14.3\mu\text{m}/24.3\mu\text{m}$ and [OIV] $25.9\mu\text{m}$ lines, known to be a signature of an AGN are stronger in the average spectra of Sy 1s than those of Sy 2s.

2. PAH emission is detected in both Sy 1s and Sy 2s, with no statistical difference in the relative strength of PAHs between the two types. This suggests that the volume responsible for the bulk of their emission is likely optically thin at $\sim 12\mu\text{m}$.

3. The $11.2\mu\text{m}$ PAH EW of the $12\mu\text{m}$ Seyfert sample correlates well with the IRAS color of the galaxies as indicated by the flux ratio of F_{25}/F_{60} . PAH emission is more suppressed in warmer galaxies, in which the strong AGN activity may destroy the PAH molecules.

4. The $9.7\mu\text{m}$ silicate feature is rather weak in Sy 1s ($S_{\text{sil}} = -0.07 \pm 0.29$) while Sy 2s mostly display silicate in absorption ($S_{\text{sil}} = -0.46 \pm 0.73$). Deep silicate absorption is observed in high luminosity Sy 2s which are classified as ULIRGs, and those with high hydrogen column density estimated from their X-ray emission.

5. The FIR luminosities of the $12\mu\text{m}$ Seyferts are dominated by star-formation. Their mid-IR luminosity increases by the additional AGN contribution. A method to estimate the AGN contribution to the $12\mu\text{m}$ luminosity, in a statistical sense, has been proposed and applied to the sample.

We would like to acknowledge L. Armus, M. Malkan, Y. Shi and M. Elvis for helpful science discussions. We thank J.D. Smith with help on the use of CUBISM to extract spectral mapping data. We would also like to thank H. Spoon and L. Hao for help in measuring the silicate features. We thank an anonymous referee whose comments help to improve this manuscript. V.C. acknowledges partial support from the EU ToK grant 39965. L.S. and

S.T. acknowledge support from the Italian Space Agency (ASI).

REFERENCES

- Antonucci, R. R. J., & Miller, J. S. 1985, *ApJ*, 297, 621
- Antonucci, R. 1993, *ARA&A*, 31, 473
- Armus, L., et al. 2004, *ApJS*, 154, 184
- Armus, L., et al. 2007, *ApJ*, 656, 148
- Bassani, L., et al. 2006, *ApJ*, 636, L65
- Bernard-Salas, J. et al. 2009, *ApJS*, submitted
- Brand, K., et al. 2006, *ApJ*, 644, 143
- Brandl, B. R., et al. 2006, *ApJ*, 653, 1129
- Buchanan, C. L., Gallimore, J. F., O’Dea, C. P., Baum, S. A., Axon, D. J., Robinson, A., Elitzur, M., & Elvis, M. 2006, *AJ*, 132, 401
- Calzetti, D., et al. 2005, *ApJ*, 633, 871
- Calzetti, D., et al. 2007, *ApJ*, 666, 870
- Charmandaris, V. 2008, *Infrared Diagnostics of Galaxy Evolution*, 381, 3
- Clavel, J., et al. 2000, *A&A*, 357, 839
- Cohen, M., Megeath, T.G., Hammersley, P.L., Martin-Luis, F., & Stauffer, J. 2003, *AJ*, 125, 2645
- Contursi, A., et al. 2000, *A&A*, 362, 310
- de Graauw, T., et al. 1996, *A&A*, 315, L49
- Deo, R. P., Crenshaw, D. M., Kraemer, S. B., Dietrich, M., Elitzur, M., Teplitz, H., & Turner, T. J. 2007, *ApJ*, 671, 124
- Desai, V., et al. 2007, *ApJ*, 669, 810
- Desert, F. X., & Dennefeld, M. 1988, *A&A*, 206, 227

- Draine, B. T. 2003, *ARA&A*, 41, 241
- Draine, B. T., & Li, A. 2001, *ApJ*, 551, 807
- Dudley, C. C., & Wynn-Williams, C. G. 1997, *ApJ*, 488, 720
- Efstathiou, A., & Rowan-Robinson, M. 1995, *MNRAS*, 273, 649
- Elitzur, M. 2008, *New Astronomy Review*, 52, 274
- Engelbracht, C. W., Rieke, G. H., Gordon, K. D., Smith, J.-D. T., Werner, M. W., Moustakas, J., Willmer, C. N. A., & Vanzi, L. 2008, *ApJ*, 678, 804
- Fadda, D., Flores, H., Hasinger, G., Franceschini, A., Altieri, B., Cesarsky, C. J., Elbaz, D., & Ferrando, P. 2002, *A&A*, 383, 838
- Farrah, D., et al. 2007, *ApJ*, 667, 149
- Förster Schreiber, N. M., Roussel, H., Sauvage, M., & Charmandaris, V. 2004, *A&A*, 419, 501
- Galliano, F., Madden, S. C., Tielens, A. G. G. M., Peeters, E., & Jones, A. P. 2008, *ApJ*, 679, 310
- Genzel, R., et al. 1998, *ApJ*, 498, 579
- Gillett, F. C., Kleinmann, D. E., Wright, E. L., & Capps, R. W. 1975, *ApJ*, 198, L65
- Gilli, R., Comastri, A., & Hasinger, G. 2007, *A&A*, 463, 79
- Gorjian, V., Cleary, K., Werner, M. W., & Lawrence, C. R. 2007, *ApJ*, 655, L73
- Hao, L., et al. 2005, *ApJ*, 625, L75
- Hao, L., Weedman, D. W., Spoon, H. W. W., Marshall, J. A., Levenson, N. A., Elitzur, M., & Houck, J. R. 2007, *ApJ*, 655, L77
- Hao, L., Wu, Y., Charmandaris, V., et al. 2009, *ApJ*, (submitted)
- Hasinger, G., Miyaji, T., & Schmidt, M. 2005, *A&A*, 441, 417
- Higdon, S. J. U., et al. 2004, *PASP*, 116, 975
- Ho, L. C. 2008, *ARA&A*, 46, 475
- Houck, J. R., et al. 2004a, *ApJS*, 154, 18

- Houck, J. R., et al. 2004b, *ApJS*, 154, 211
- Houck, J. R., et al. 2005, *ApJ*, 622, 105
- Kennicutt, R. C., Jr. 1998, *ARA&A*, 36, 189
- Kennicutt, R. C., Jr., et al. 2003, *PASP*, 115, 928
- Laurent, O., Mirabel, I. F., Charmandaris, V., Gallais, P., Madden, S. C., Sauvage, M., Vigroux, L., & Cesarsky, C. 2000, *A&A*, 359, 887
- Le Flocc'h, E., et al. 2005, *ApJ*, 632, 169
- Li, M. P., Shi, Q. J., & Li, A. 2008, *MNRAS*, 391, L49
- Lutz, D., Maiolino, R., Spoon, H. W. W., & Moorwood, A. F. M. 2004, *A&A*, 418, 465
- Lutz, D., Spoon, H. W. W., Rigopoulou, D., Moorwood, A. F. M., & Genzel, R. 1998, *ApJ*, 505, L103
- Maiolino, R., Salvati, M., Bassani, L., Dadina, M., della Ceca, R., Matt, G., Risaliti, G., & Zamorani, G. 1998, *A&A*, 338, 781
- Markwardt, C. B., Tueller, J., Skinner, G. K., Gehrels, N., Barthelmy, S. D., & Mushotzky, R. F. 2005, *ApJ*, 633, L77
- Meléndez, M., et al. 2008a, *ApJ*, 682, 94
- Meléndez, M., Kraemer, S. B., Schmitt, H. R., Crenshaw, D. M., Deo, R. P., Mushotzky, R. F., & Bruhweiler, F. C. 2008b, *ApJ*, 689, 95
- Nardini, E., Risaliti, G., Salvati, M., Sani, E., Imanishi, M., Marconi, A., & Maiolino, R. 2008, *MNRAS*, 385, L130
- Nenkova, M., Sirocky, M. M., Nikutta, R., Ivezić, Ž., & Elitzur, M. 2008, *ApJ*, 685, 160
- Peeters, E., Hony, S., Van Kerckhoven, C., Tielens, A. G. G. M., Allamandola, L. J., Hudgins, D. M., & Bauschlicher, C. W. 2002, *A&A*, 390, 1089
- Peeters, E., Spoon, H. W. W., & Tielens, A. G. G. M. 2004, *ApJ*, 613, 986
- Rieke, G. H., & Low, F. J. 1975, *ApJ*, 199, L13
- Roche, P. F., Aitken, D. K., Smith, C. H., & Ward, M. J. 1991, *MNRAS*, 248, 606

- Rush, B., Malkan, M. A., & Spinoglio, L. 1993, *ApJS*, 89, 1
- Sajina, A., Yan, L., Armus, L., Choi, P., Fadda, D., Helou, G., & Spoon, H. 2007, *ApJ*, 664, 713
- Sanders, D. B., Soifer, B. T., Elias, J. H., Neugebauer, G., & Matthews, K. 1988, *ApJ*, 328, L35
- Sanders, D. B., & Mirabel, I. F. 1996, *ARA&A*, 34, 749
- Sanders, D. B., Mazzarella, J. M., Kim, D.-C., Surace, J. A., & Soifer, B. T. 2003, *AJ*, 126, 1607
- Sazonov, S., Revnivtsev, M., Krivonos, R., Churazov, E., & Sunyaev, R. 2007, *A&A*, 462, 57
- Schaerer, D., & Stasińska, G. 1999, *A&A*, 345, L17
- Shi, Y., et al. 2007, *ApJ*, 669, 841
- Shu, X. W., Wang, J. X., Jiang, P., Fan, L. L., & Wang, T. G. 2007, *ApJ*, 657, 167
- Siebenmorgen, R., Haas, M., Krügel, E., & Schulz, B. 2005, *A&A*, 436, L5
- Sirocky, M. M., Levenson, N. A., Elitzur, M., Spoon, H. W. W., & Armus, L. 2008, *ApJ*, 678, 729
- Smith, J. D. T., et al. 2007a, *ApJ*, 656, 770
- Smith, J. D. T., et al., 2007b, *PASP*, 119, 1133
- Spinoglio, L., & Malkan, M. A. 1989, *ApJ*, 342, 83
- Spinoglio, L., Malkan, M. A., Rush, B., Carrasco, L., & Recillas-Cruz, E. 1995, *ApJ*, 453, 616
- Spoon, H. W. W., Marshall, J. A., Houck, J. R., Elitzur, M., Hao, L., Armus, L., Brandl, B. R., & Charmandaris, V. 2007, *ApJ*, 654, L49
- Stern, D., et al. 2005, *ApJ*, 631, 163
- Sturm, E., Lutz, D., Verma, A., Netzer, H., Sternberg, A., Moorwood, A. F. M., Oliva, E., & Genzel, R. 2002, *A&A*, 393, 821
- Sturm, E., et al. 2005, *ApJ*, 629, L21

- Sturm, E., et al. 2006, *ApJ*, 653, L13
- Teplitz, H. I., et al. 2007, *ApJ*, 659, 941
- Thompson, G. D., Levenson, N. A., Uddin, S. A., & Sirocky, M. M. 2009, *ApJ*, 697, 182
- Tommasin, S., Spinoglio, L., Malkan, M. A., Smith, H., González-Alfonso, E., & Charmandaris, V. 2008, *ApJ*, 676, 836
- Urry, C. M., & Padovani, P. 1995, *PASP*, 107, 803
- van Dishoeck, E. F. 2004, *ARA&A*, 42, 119
- Verma, A., Charmandaris, V., Klaas, U., Lutz, D., & Haas, M. 2005, *Space Science Reviews*, 119, 355
- Voit, G. M. 1992, *MNRAS*, 258, 84
- Weedman, D. W., et al. 2005, *ApJ*, 633, 706
- Weedman, D., et al. 2006, *ApJ*, 653, 101
- Weedman, D. & Houck, J. R., 2008, *ApJ*, 686, 127
- Werner, M. W., et al. 2004, *ApJS*, 154, 1
- Worsley, M. A., et al. 2005, *MNRAS*, 357, 1281
- Wu, H., Cao, C., Hao, C.-N., Liu, F.-S., Wang, J.-L., Xia, X.-Y., Deng, Z.-G., & Young, C. K.-S. 2005, *ApJ*, 632, L79
- Yan, L., et al. 2005, *ApJ*, 628, 604

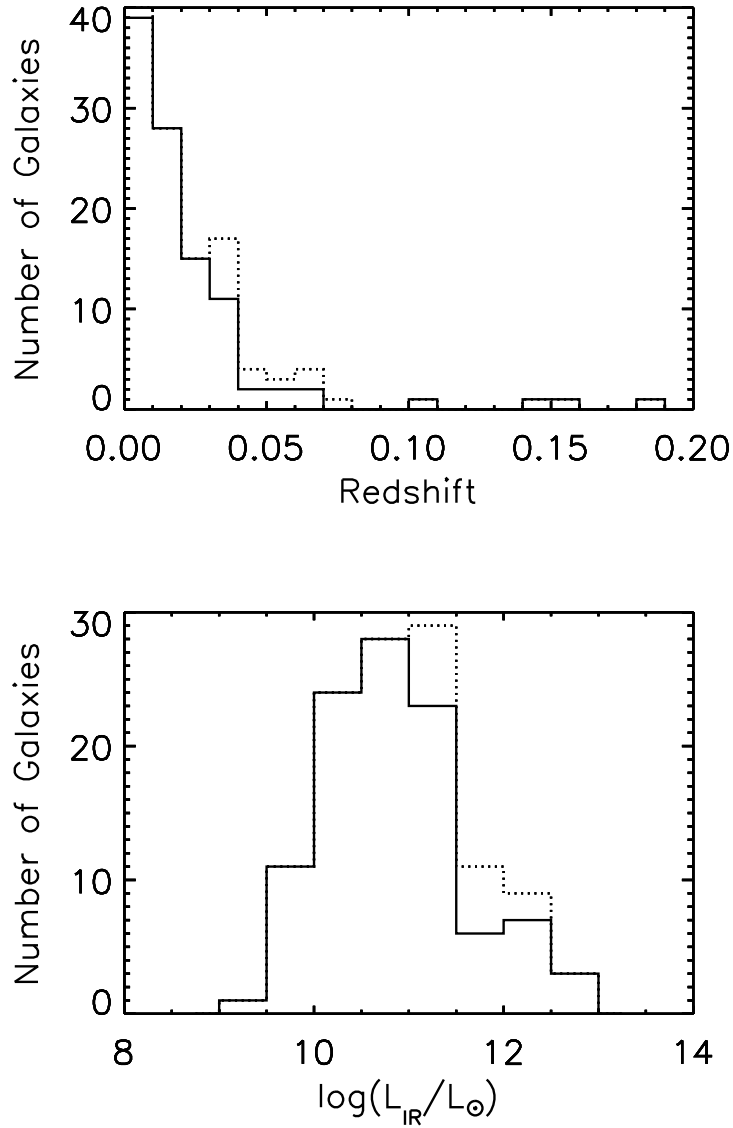


Fig. 1.— a) The redshift distribution of the $12\mu\text{m}$ Seyfert sample (dotted line) and those with available IRS data studied in this paper (solid line). b) The luminosity distribution of the $12\mu\text{m}$ Seyfert sample (dotted line) and those with available IRS data studied in this paper (solid line).

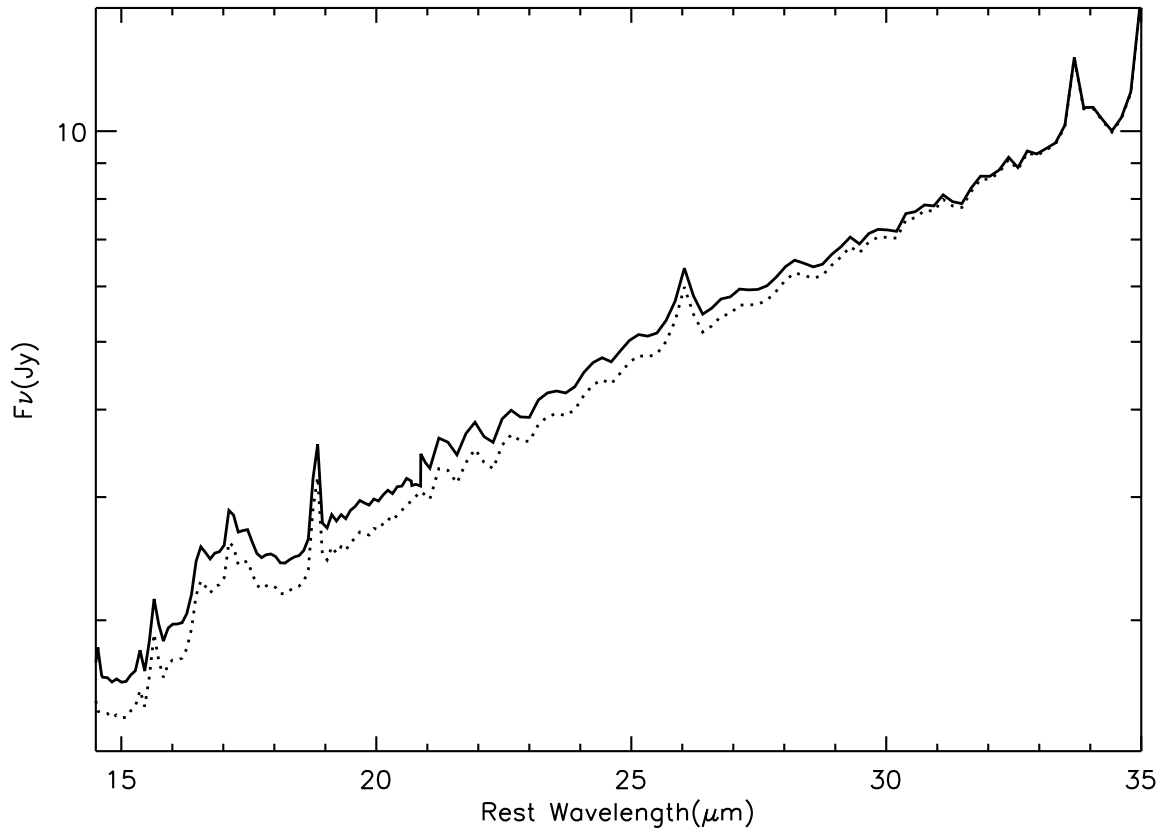


Fig. 2.— A comparison of the LL spectra of NGC1365. The solid and dotted line is before and after applying the image convolution method.

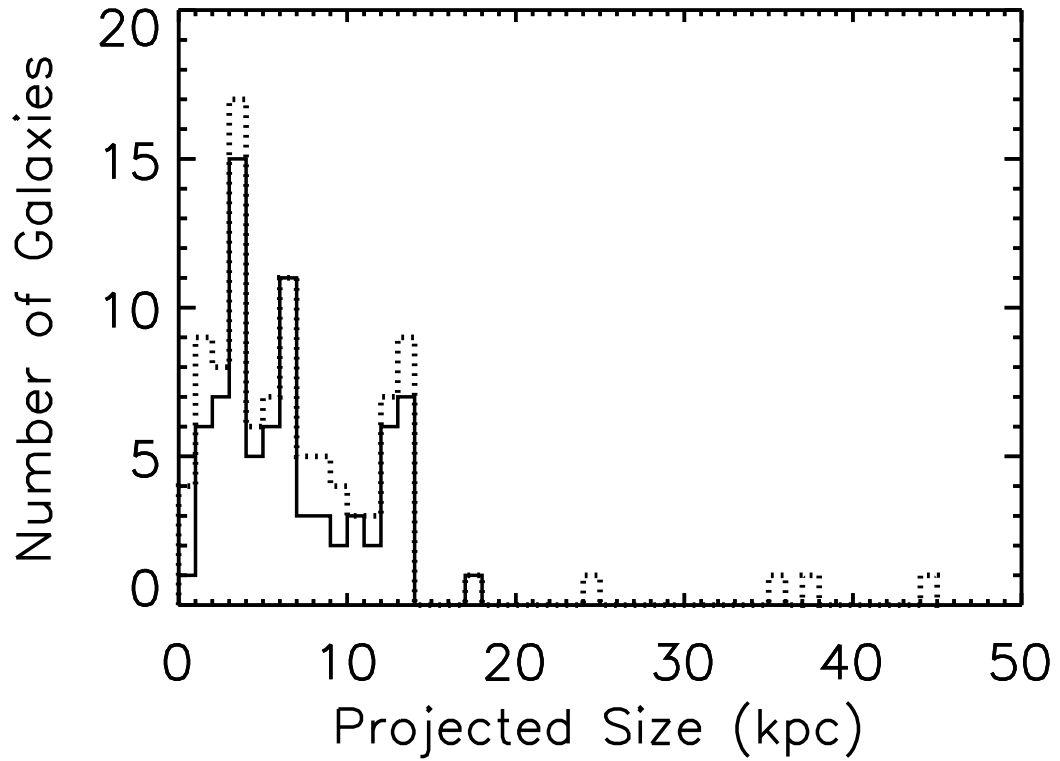


Fig. 3.— A histogram of the projected linear size of the IRS spectral extraction aperture at the distance of the corresponding target of the $12\mu\text{m}$ Seyfert sample. The dotted line indicates the distribution of the whole sample, while the solid line indicates the distribution for those that have been observed using the spectral mapping mode.

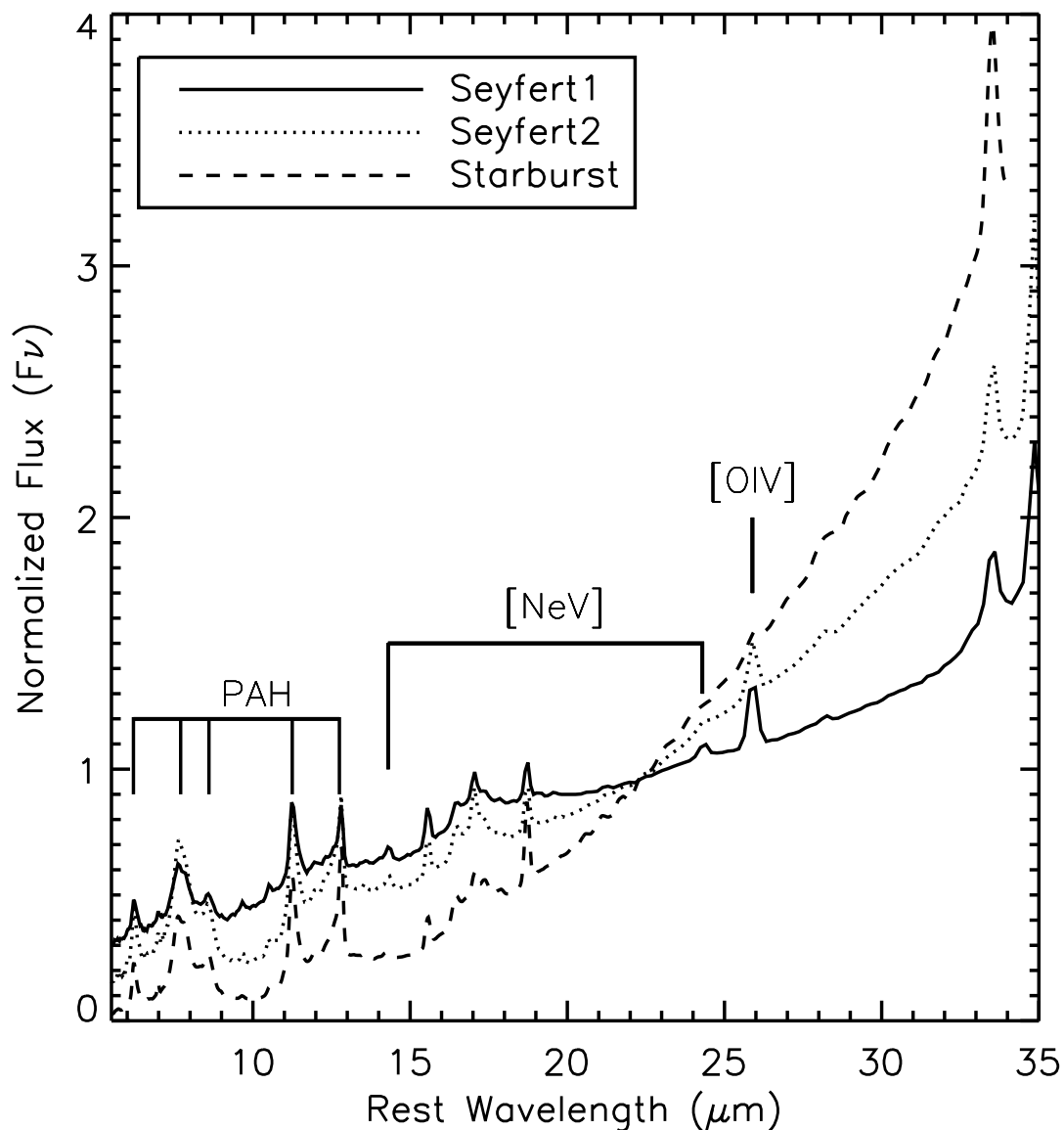


Fig. 4.— A comparison among the average mid-IR spectrum of Sy 1s (solid line) and Sy 2s (dotted line) of the 12 μm sample, as well as the starbursts (dashed line) of Brandl et al. (2006). All spectra have been normalized at 22 μm . Note that the high-ionization fine-structure lines of [OIV] 25.89 μm are present in all three spectra, while [NeV] 14.3/24.3 μm are only present in the average spectra of the two Seyfert types.

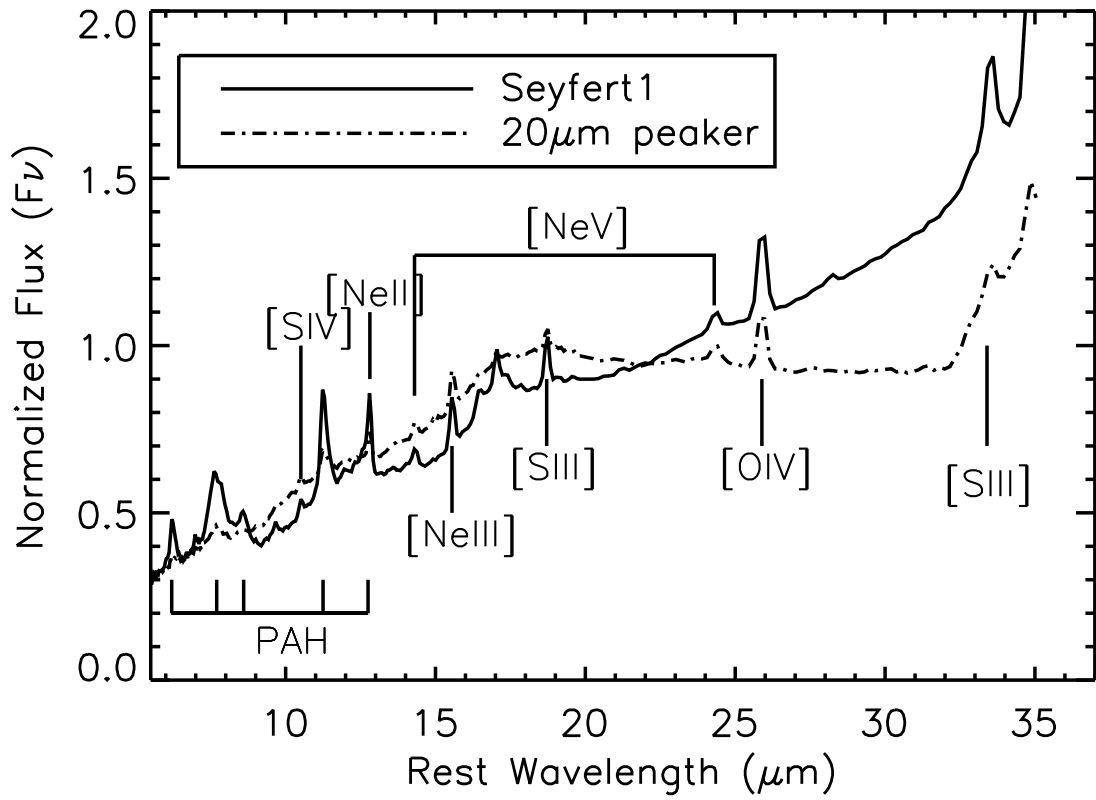


Fig. 5.— A comparison between the average mid-IR spectrum of “20 μm peakers” (dash-dotted line) and Sy 1s (solid line) of our sample. All spectra have been normalized at 22 μm .

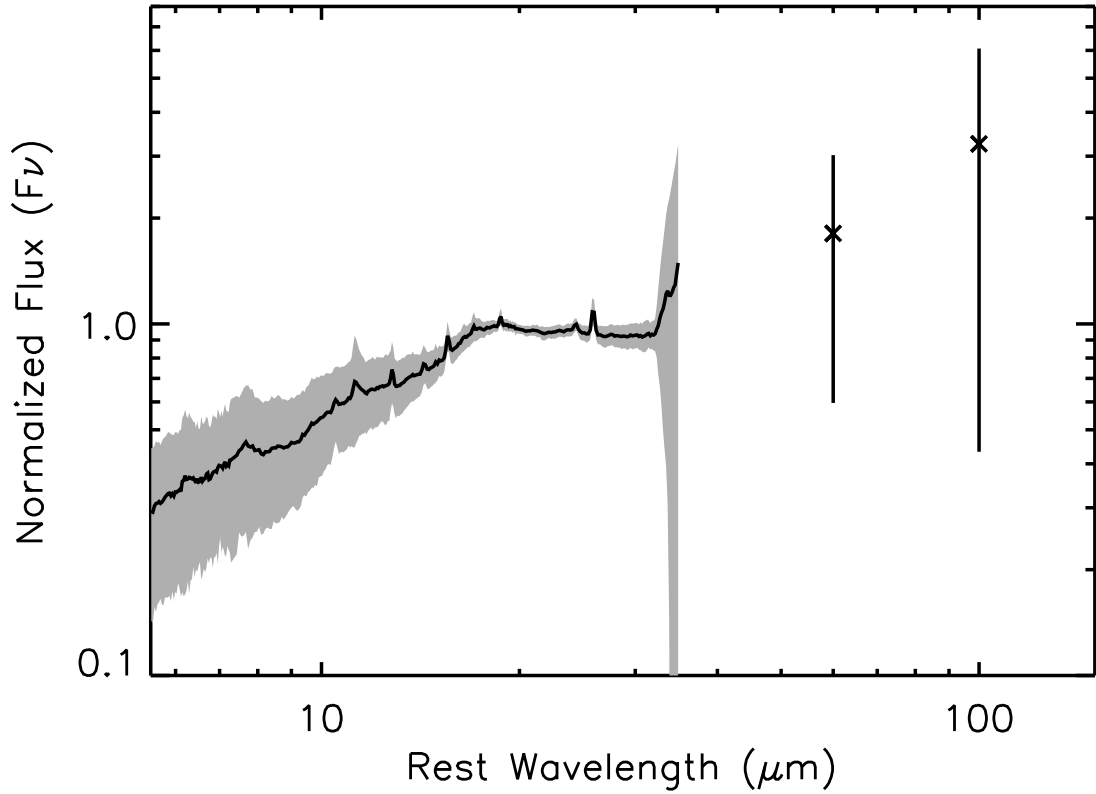


Fig. 6.— The global IR spectral energy distribution of the “20 μm peakers” after normalizing at 22 μm . The two data points at 60 and 100 μm have been obtained by averaging the IRAS 60 and 100 μm fluxes after normalization. The grey zone in the spectrum and the error bars indicate the 1- σ scatter of the averaged values.

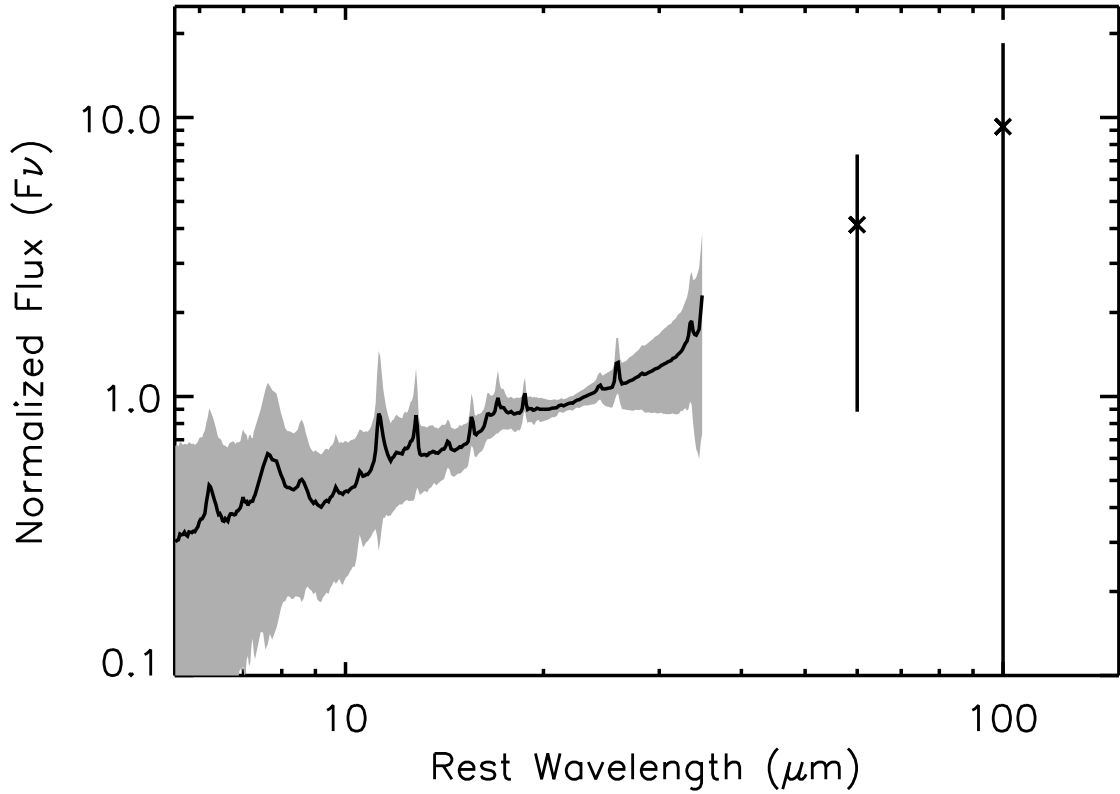


Fig. 7.— The average IR spectral energy distribution of the Seyfert 1 galaxies after normalizing at $22\ \mu\text{m}$. The two data points at 60 and $100\ \mu\text{m}$ have been obtained by averaging the IRAS 60 and $100\ \mu\text{m}$ fluxes after normalization. The grey zone in the spectrum and the error bars indicate the $1\text{-}\sigma$ scatter of the averaged values.

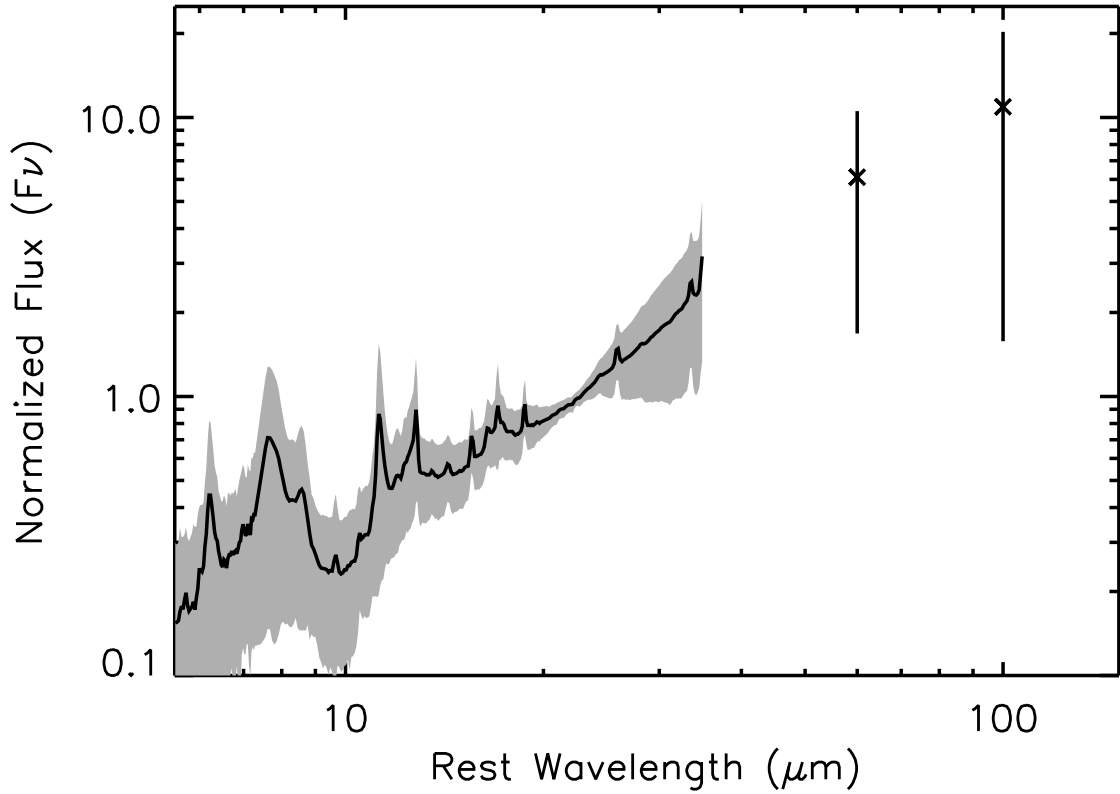


Fig. 8.— The average IR spectral energy distribution of the Seyfert 2 galaxies after normalizing at $22 \mu\text{m}$. The two data points at 60 and $100 \mu\text{m}$ have been obtained by averaging the IRAS 60 and $100 \mu\text{m}$ fluxes after normalization. The grey zone in the spectrum and the error bars indicate the $1\text{-}\sigma$ scatter of the averaged values.

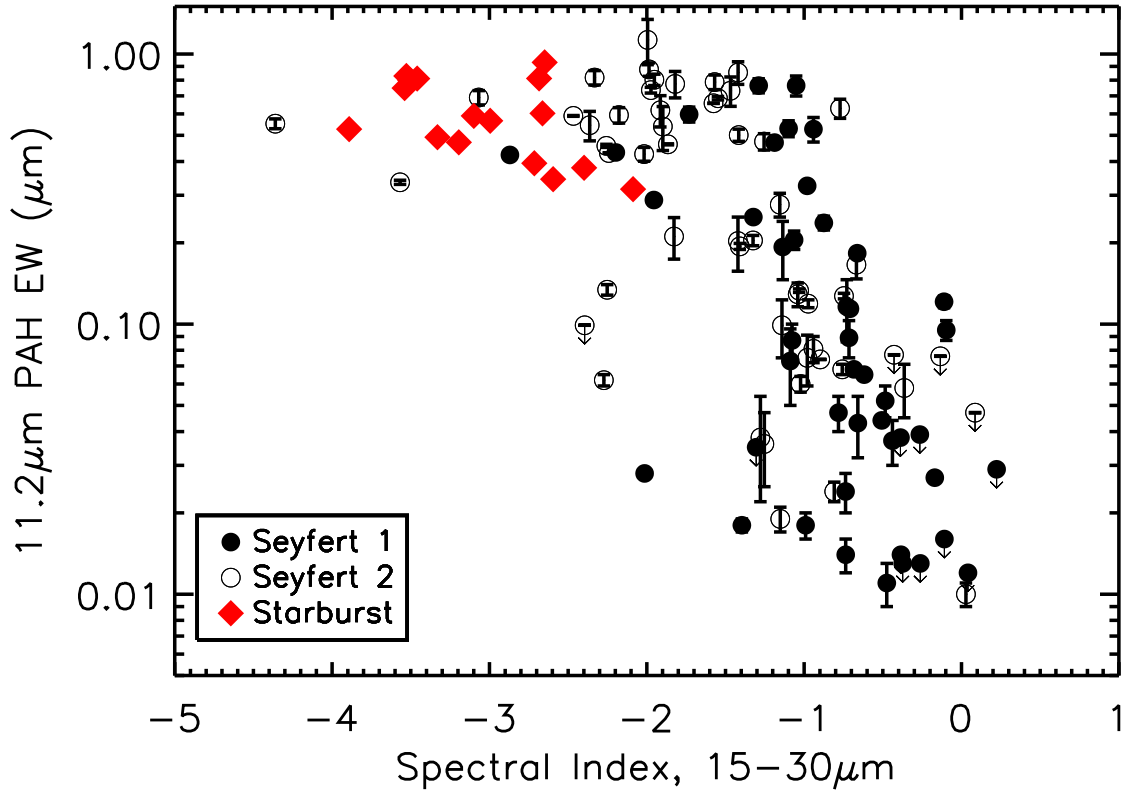


Fig. 9.— The 15-30 μm spectral index vs 11.2 μm PAH EW for the 12 μm Seyfert sample. The filled circles are Seyfert 1s, the open circles are Seyfert 2s, while the diamonds denote the starburst galaxies from Brandl et al. (2006). Note that the PAH EWs of Seyferts are progressively suppressed as their 15 to 30 μm continuum slopes flatten.

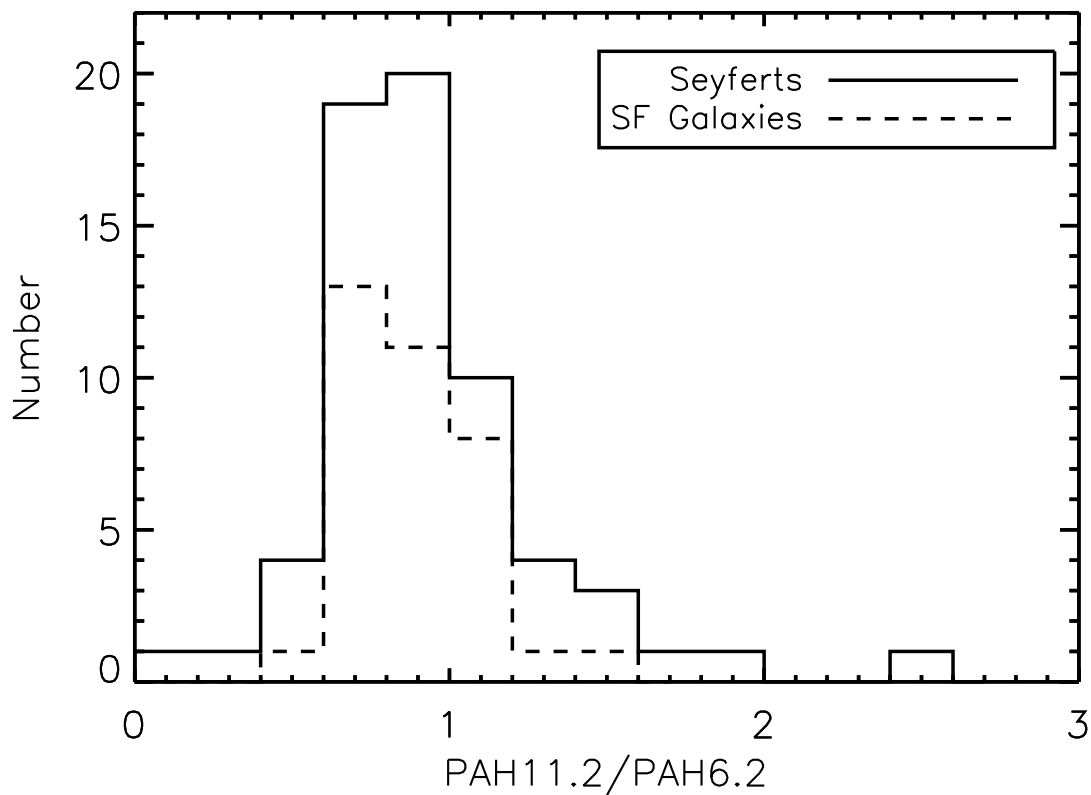


Fig. 10.— A histogram of the flux ratio of the 11.2 μm PAH to the 6.2 μm PAH feature. The solid line indicates the values of the 12 μm Seyfert sample while the dashed line indicates those of the SF galaxies from the Brandl et al. (2006) and Smith et al. (2007a). Galaxies with only upper limits measured for the aromatic features are excluded from this plot. Both the SF galaxies and the Seyferts appear to have similar distribution of the 11.2 μm/6.2 μm PAH flux ratios, indicating that globally the chemical structure of the aromatic features observed in Seyfert nuclei are likely very similar to those seen in SF galaxies.

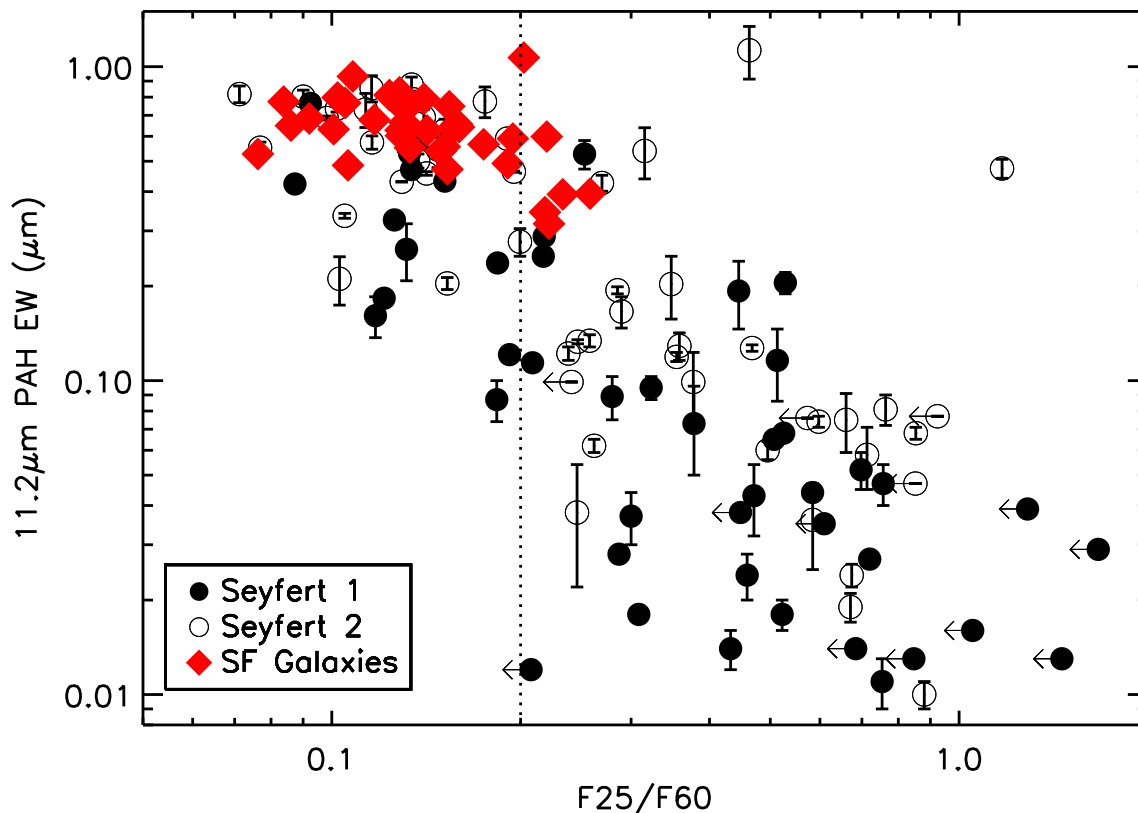


Fig. 11.— The IRAS 25 to 60 μm flux ratio (F_{25}/F_{60}) as a function of the 11.2 μm PAH EW for the 12 μm Seyfert sample. The filled circles are Sy 1s, and the open circles are Sy 2s. The diamonds represent the SF galaxies from Brandl et al. (2006) and Smith et al. (2007a). The dotted line separates the warm and cold sources based on their IRAS colors. Note that the 11.2 μm PAH EWs appear to anti-correlate with the dust temperature, as indicated by the ratio of F_{25}/F_{60} .

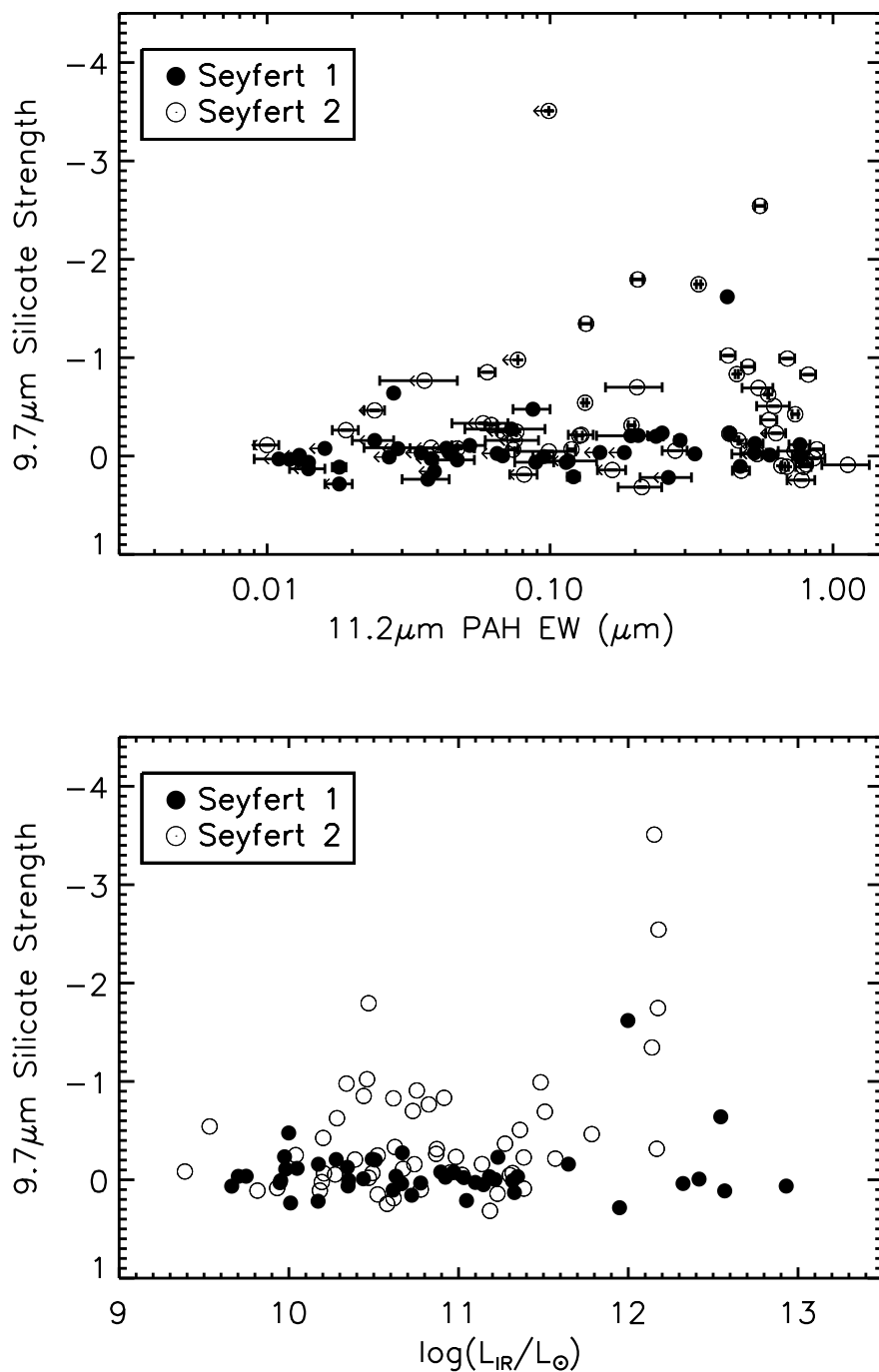


Fig. 12.— a) Top panel: Plot of the silicate strength at $9.7\ \mu\text{m}$ as a function of the PAH $11.2\ \mu\text{m}$ EW for the $12\ \mu\text{m}$ Seyfert sample. Upper limits are indicated with arrows. b) Bottom panel: The IR luminosity vs the $9.7\ \mu\text{m}$ silicate strength. The symbols are defined in the same way as Figure 11. Note that Sy 2s display a larger range in possible values of Silicate strength than Sy 1s.

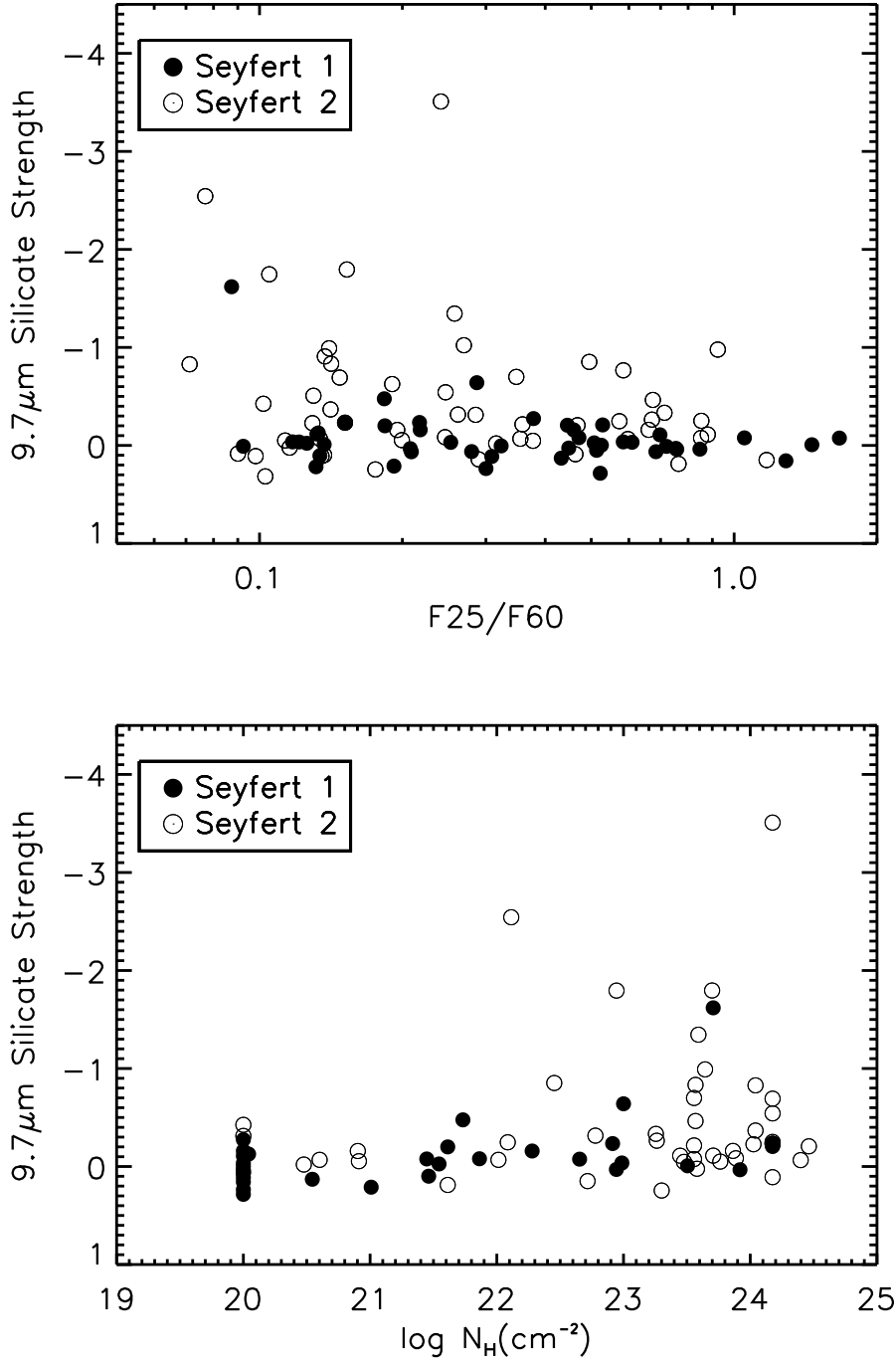


Fig. 13.— a) Top panel: The silicate strength at $9.7\ \mu\text{m}$ as a function of the galaxy color as indicated by the ratio of F25/F60. b) Bottom panel: The $9.7\ \mu\text{m}$ silicate strength versus hydrogen column density, as measured from the X-rays. The symbols are defined in the same way as Figure 11.

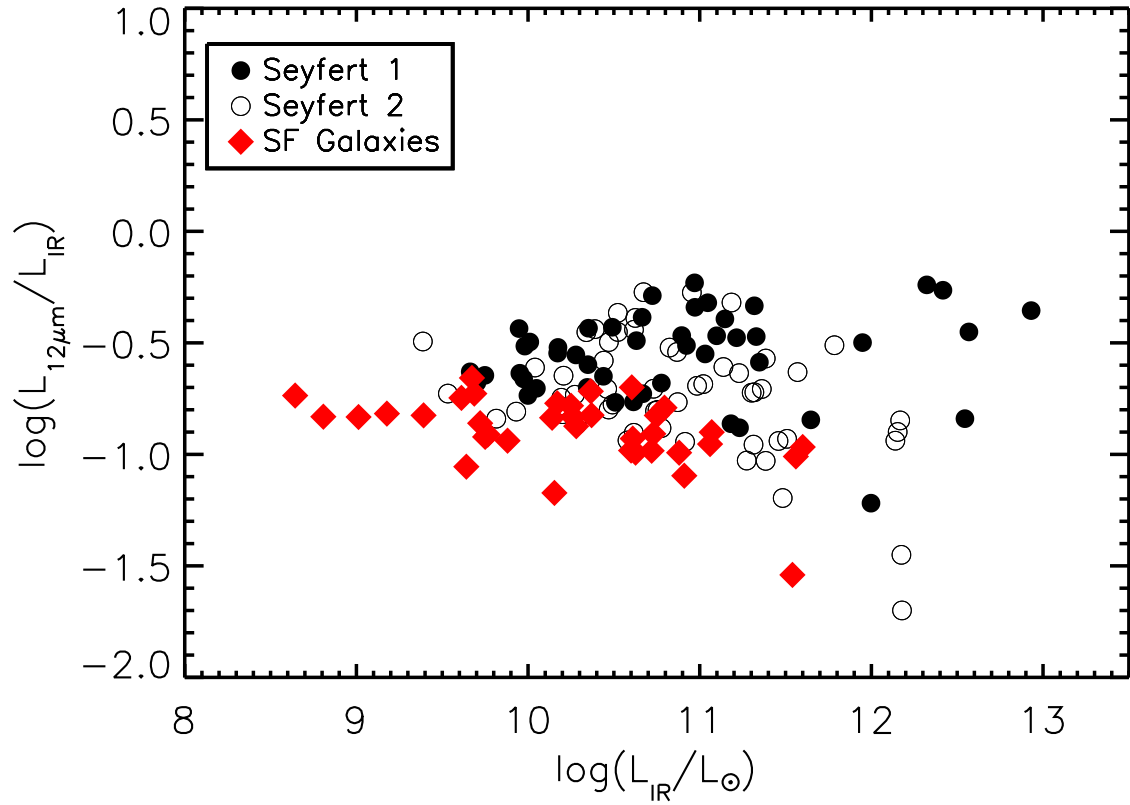


Fig. 14.— The ratio of $L_{12\mu\text{m}}/L_{\text{IR}}$ versus the total infrared luminosity of the $12\mu\text{m}$ Seyfert sample and SF galaxies. For SF galaxies, their $L_{12\mu\text{m}}$ appear to account for a nearly constant fraction of the total infrared luminosity. For Seyfert galaxies, their $L_{12\mu\text{m}}/L_{\text{IR}}$ ratios are higher than SF galaxies, and the scatter is also larger. The symbols are defined in the same way as Figure 11.

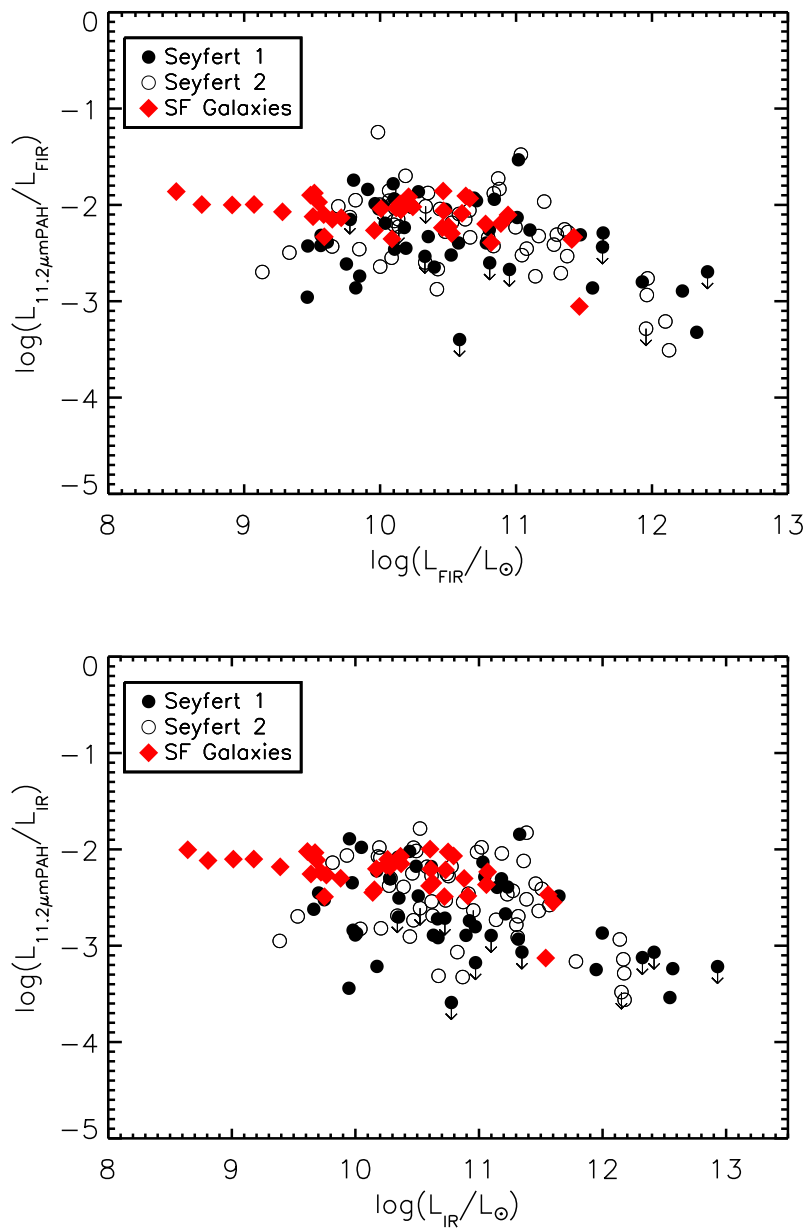


Fig. 15.— a) The $L_{11.2\mu\text{mPAH}}/L_{\text{FIR}}$ versus the FIR luminosity of the 12 μm Seyfert sample. b) Same as in a), but for the $L_{11.2\mu\text{mPAH}}/L_{\text{IR}}$ versus the total IR luminosity. Both the SF galaxies and the Seyferts appear to have a constant ratio of $L_{11.2\mu\text{mPAH}}/L_{\text{FIR}}$ and $L_{11.2\mu\text{mPAH}}/L_{\text{IR}}$, though the Seyferts appear to have a lower fraction in $L_{11.2\mu\text{mPAH}}/L_{\text{IR}}$. The symbols are defined in the same way as Figure 11.

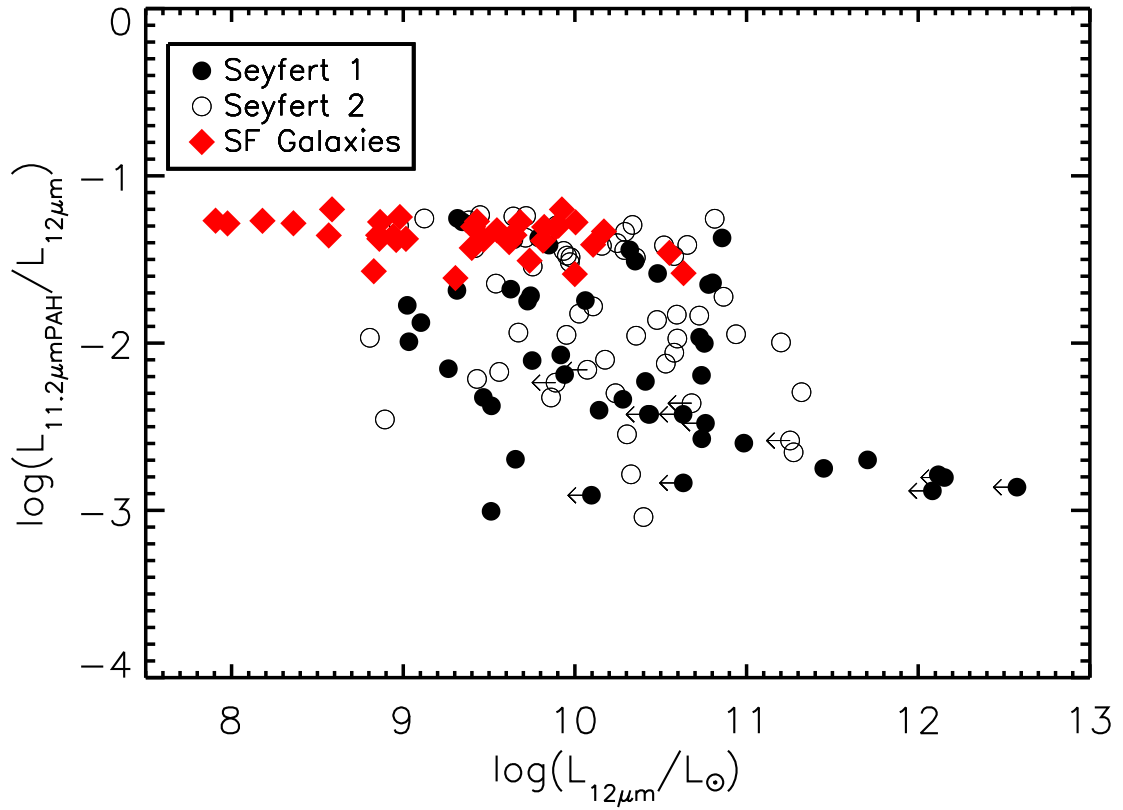


Fig. 16.— The $L_{11.2\mu\text{mPAH}}/L_{12\mu\text{m}}$ versus the IRAS $12\mu\text{m}$ luminosity of the $12\mu\text{m}$ Seyfert sample. The SF galaxies have a nearly constant ratio of $L_{11.2\mu\text{mPAH}}/L_{12\mu\text{m}}$, while the Seyferts have more scatter. The symbols are defined in the same way as Figure 11.

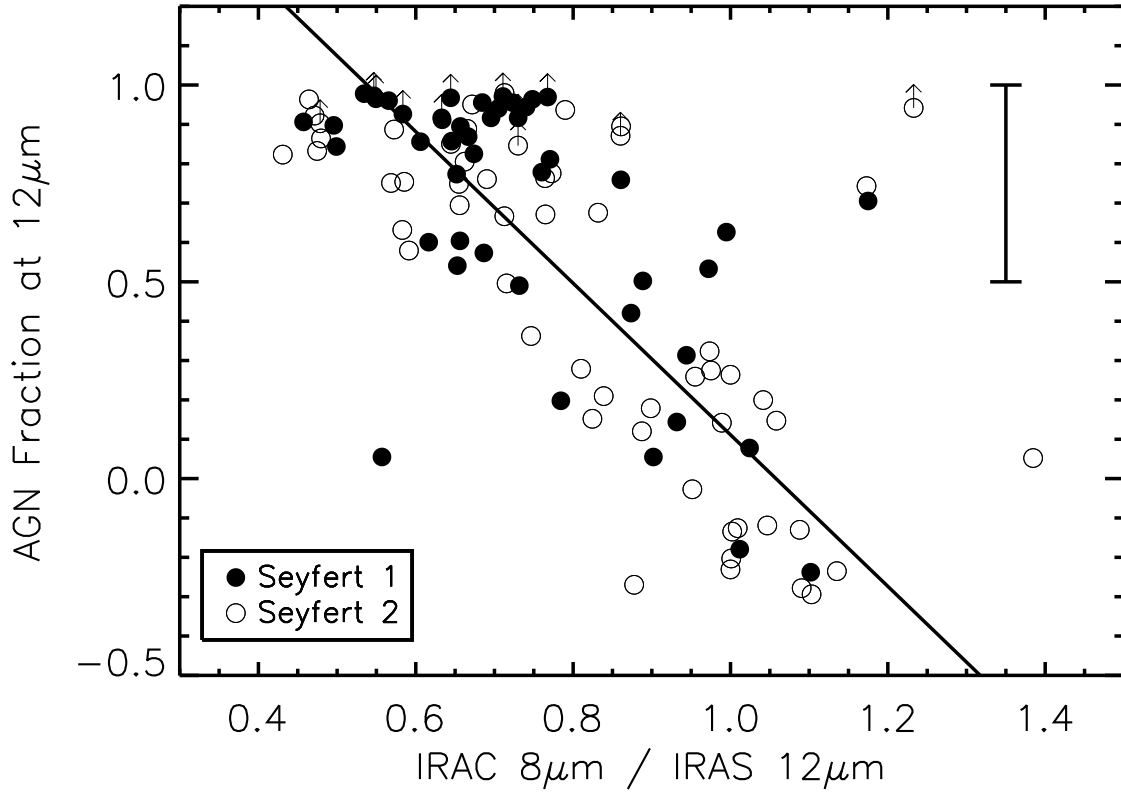


Fig. 17.— The AGN fraction (as defined in the text) at $12\mu\text{m}$ as a function of the IRAC $8\mu\text{m}$ to *IRAS* $12\mu\text{m}$ flux ratio. The Seyfert 1s are represented with filled circles and the Seyfert 2s are indicated with open circles. The solid line is a fit to the Seyfert galaxies excluding those with lower limits for the AGN fraction. The uncertainty on the “AGN fraction” is $\sim 25\%$, as indicated at the top right corner of the plot.

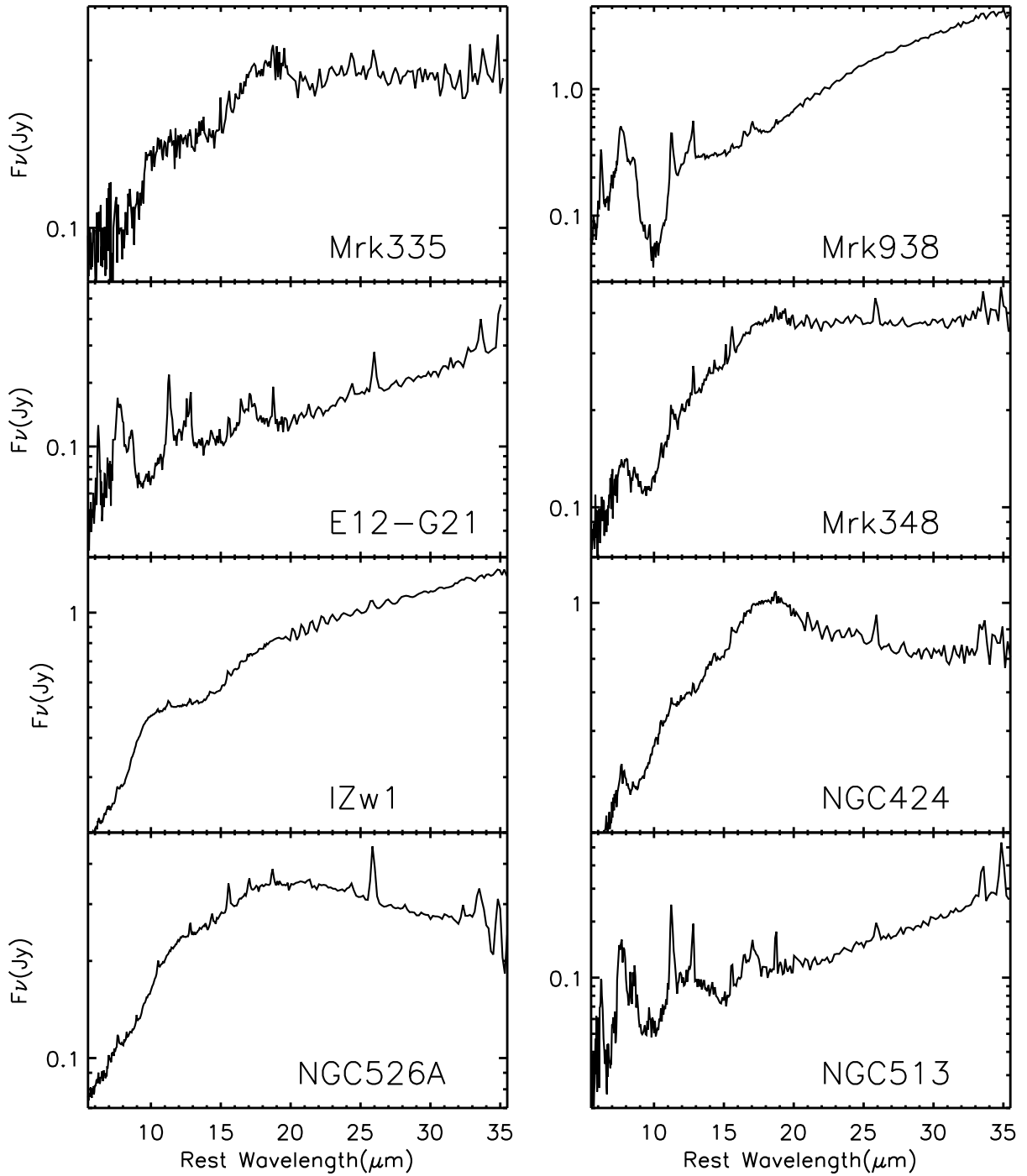


Fig. 18.— An Atlas of the Spitzer/IRS low-resolution 5-35 μm spectra of the 12 μm Seyfert sample.

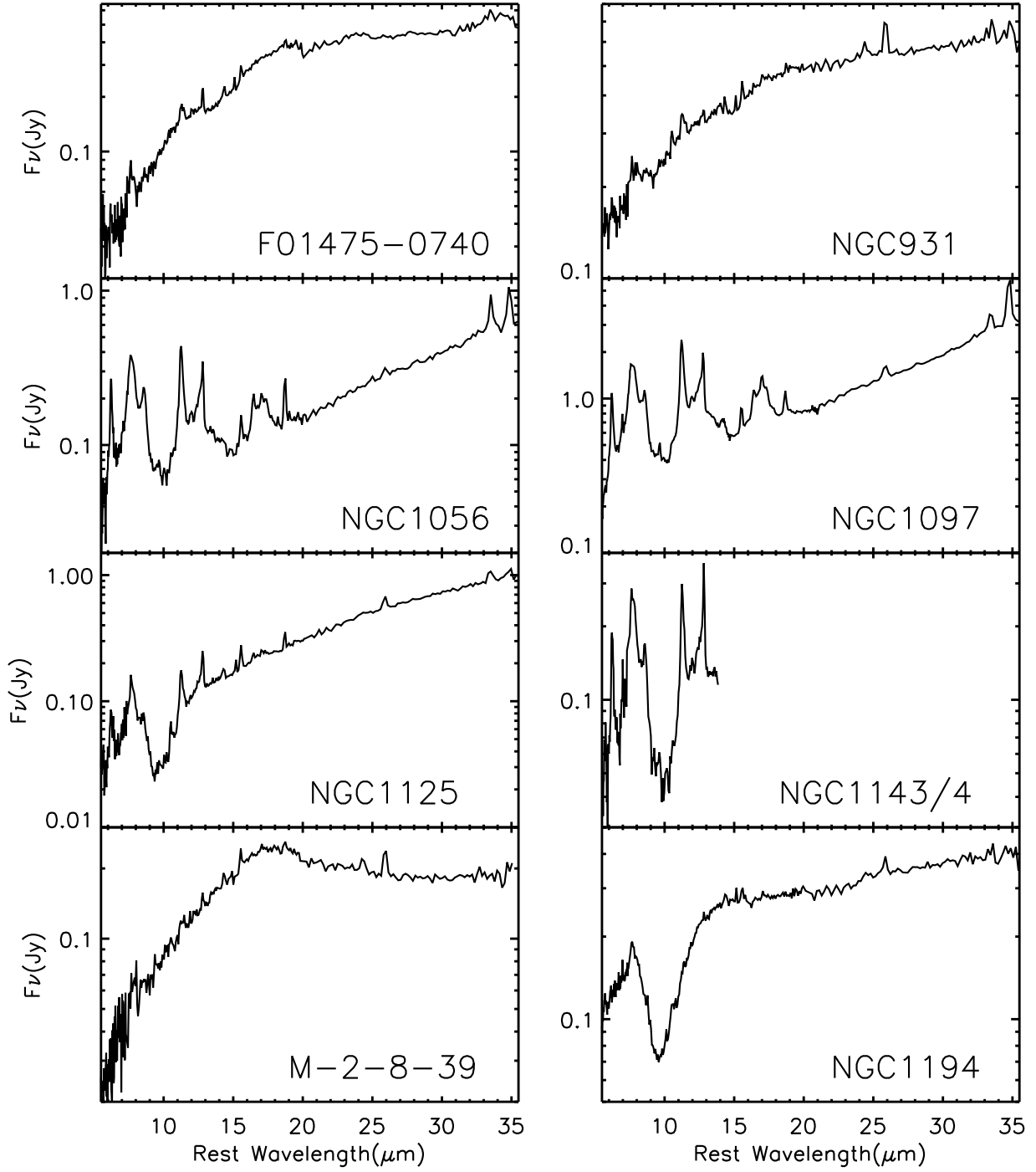


Fig. 18.— Continued.

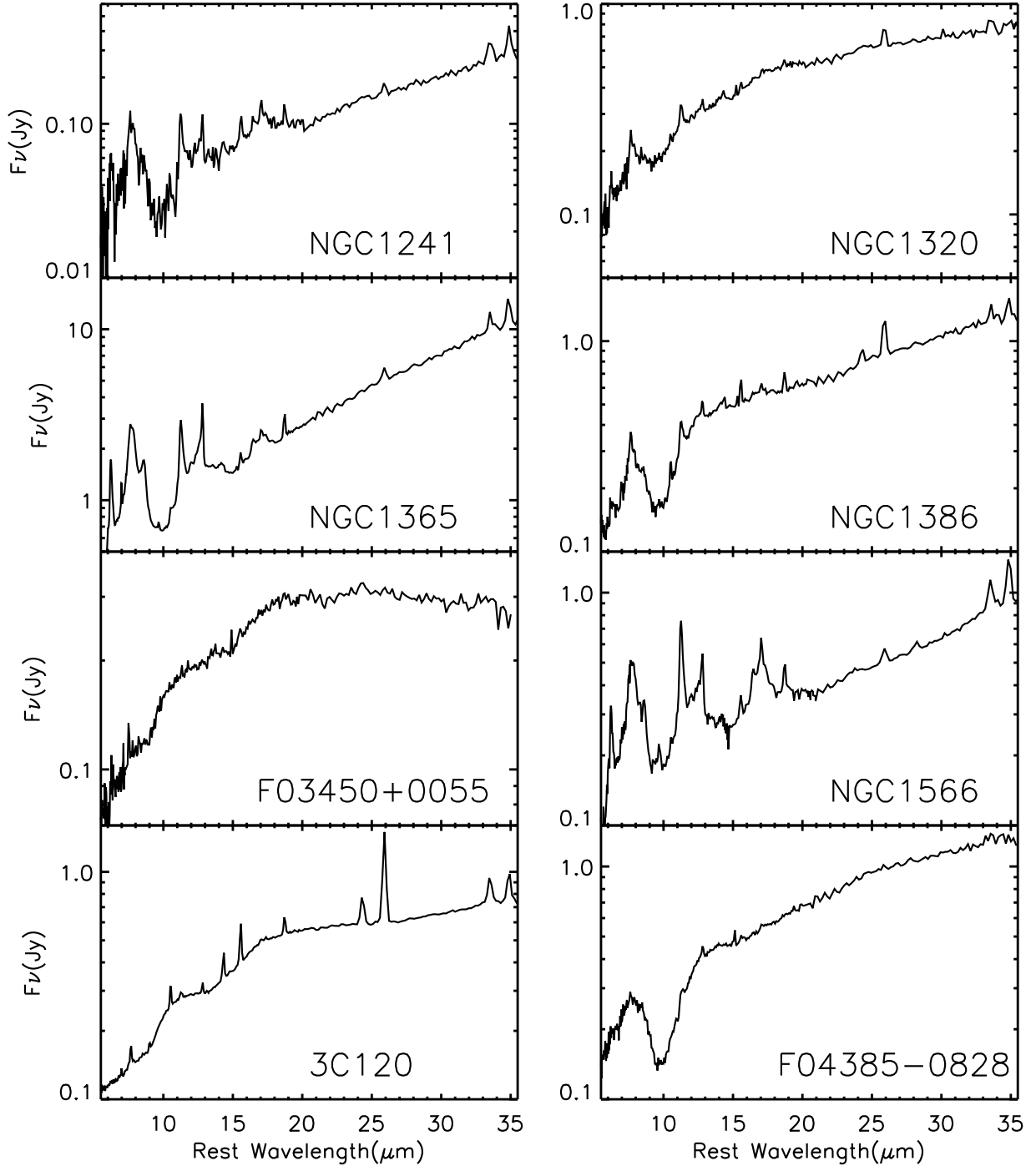


Fig. 18.— Continued.

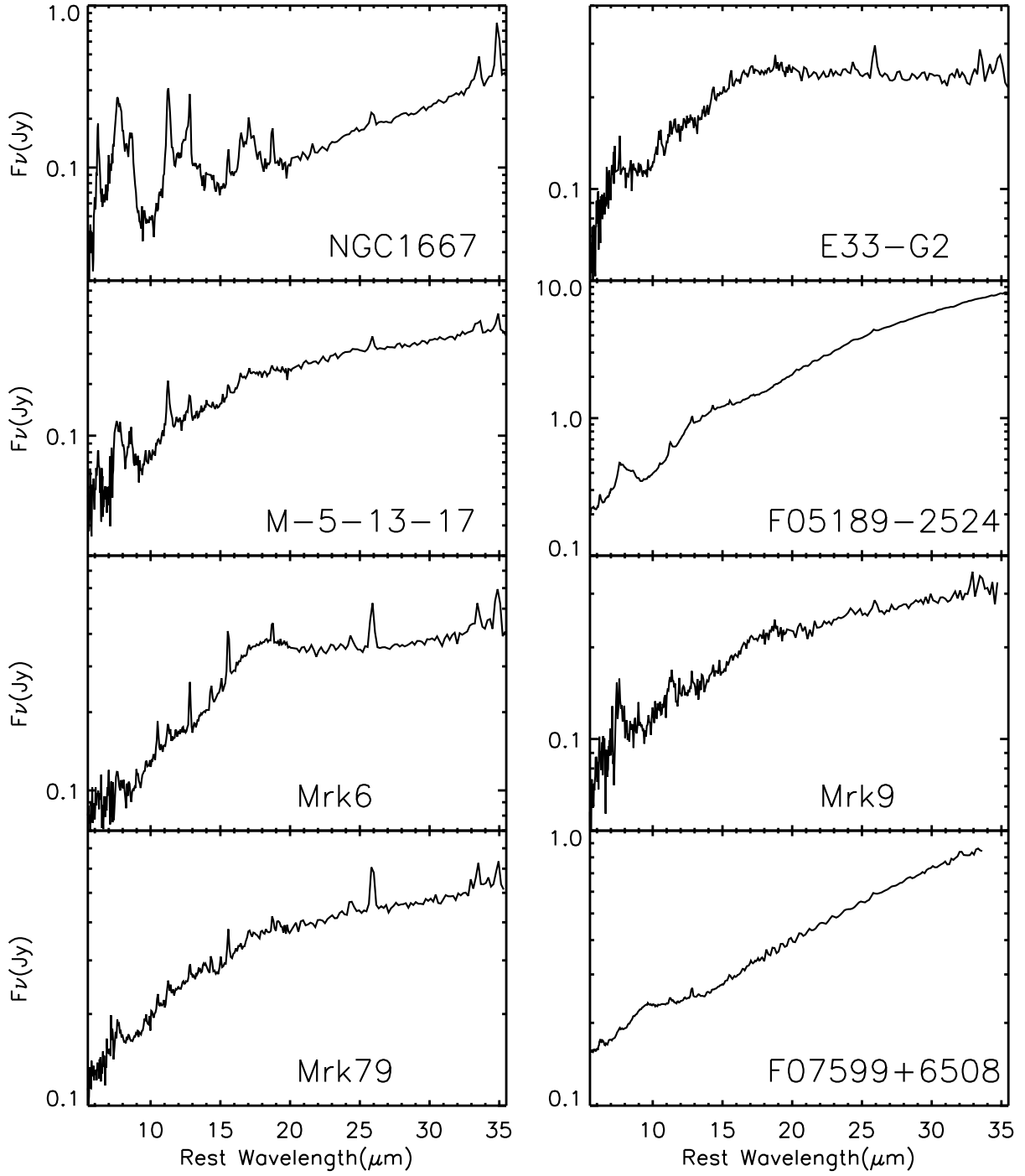


Fig. 18.— Continued.

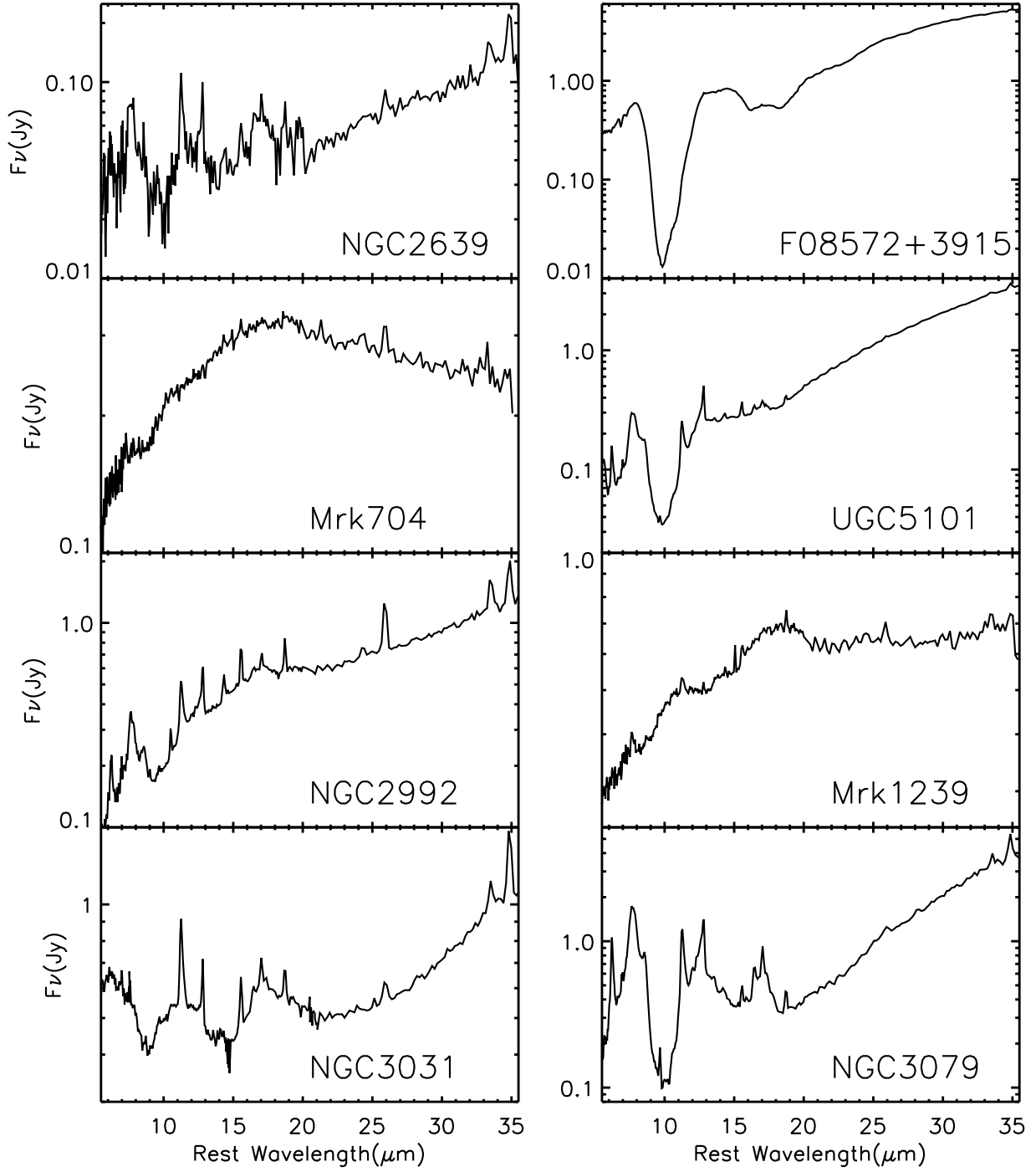


Fig. 18.— Continued.

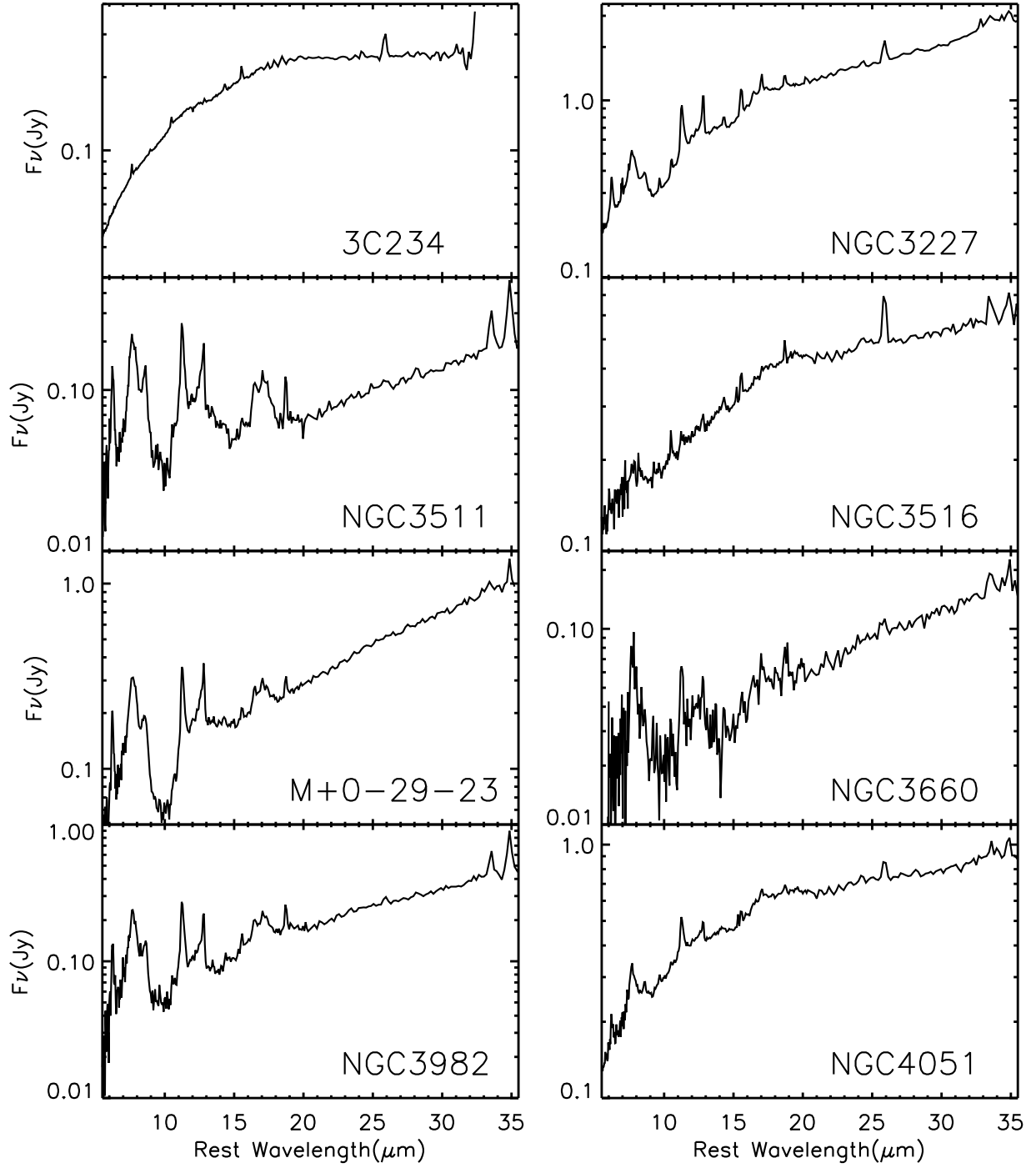


Fig. 18.— Continued.

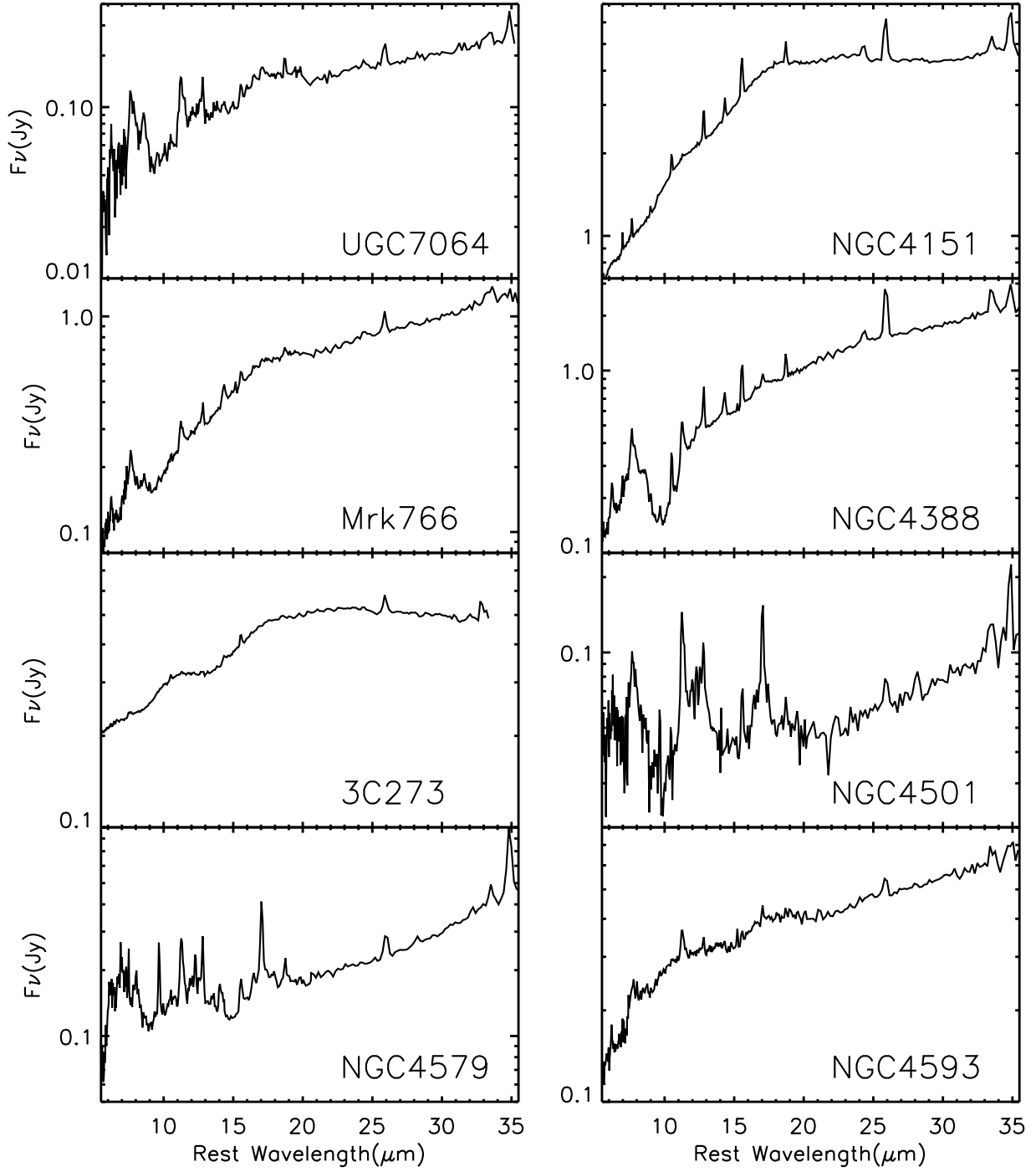


Fig. 18.— Continued.

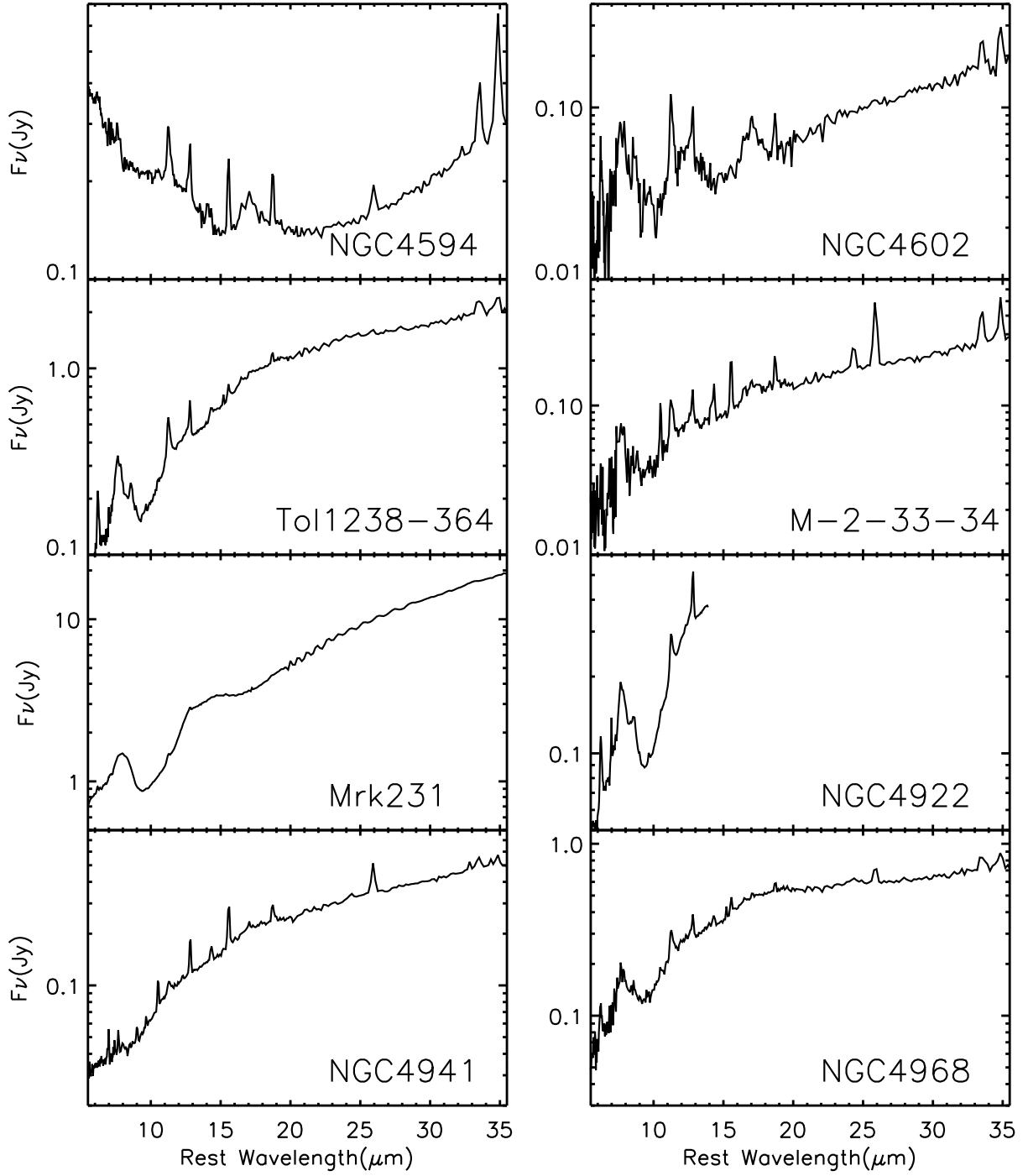


Fig. 18.— Continued.

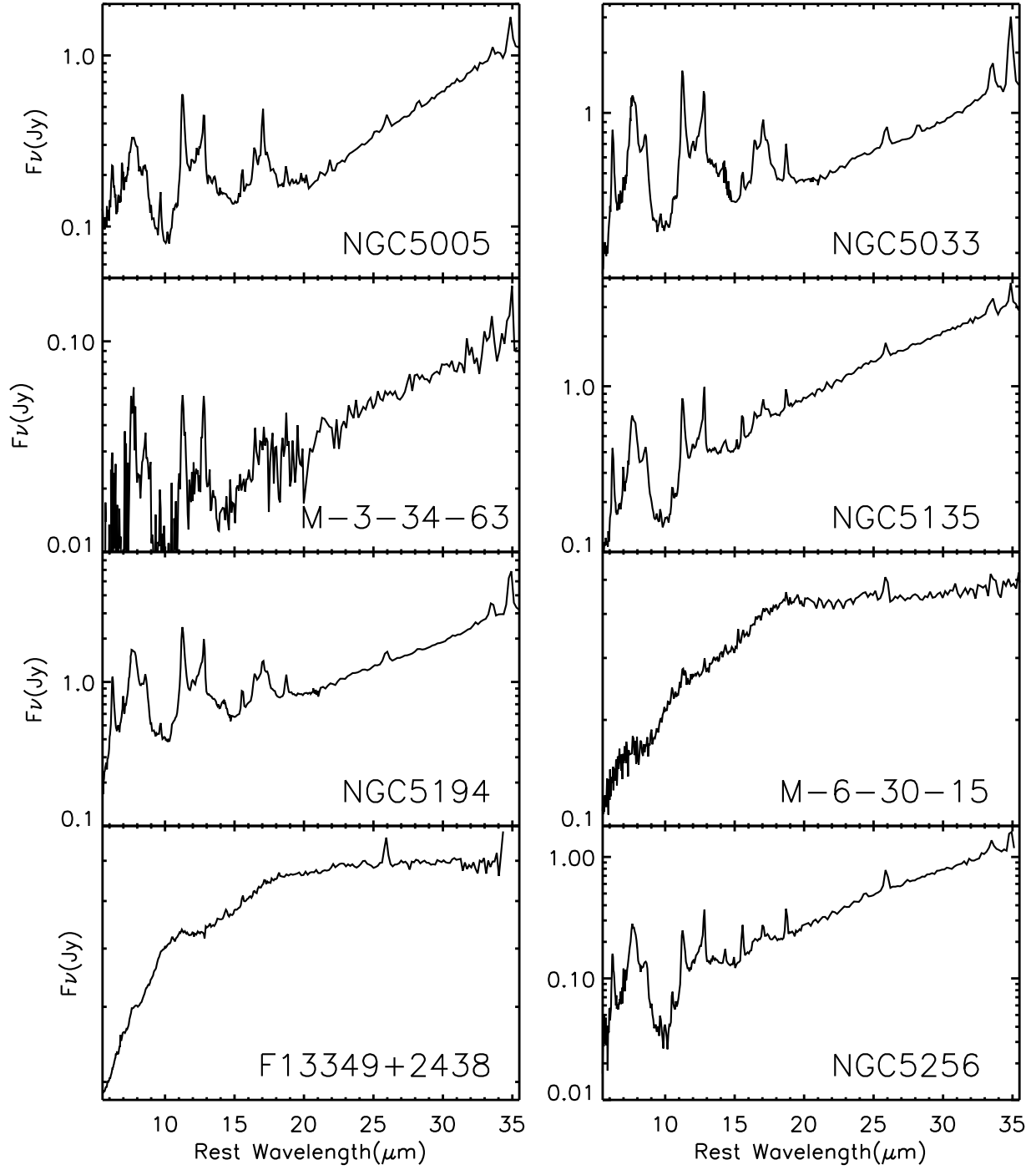


Fig. 18.— Continued.

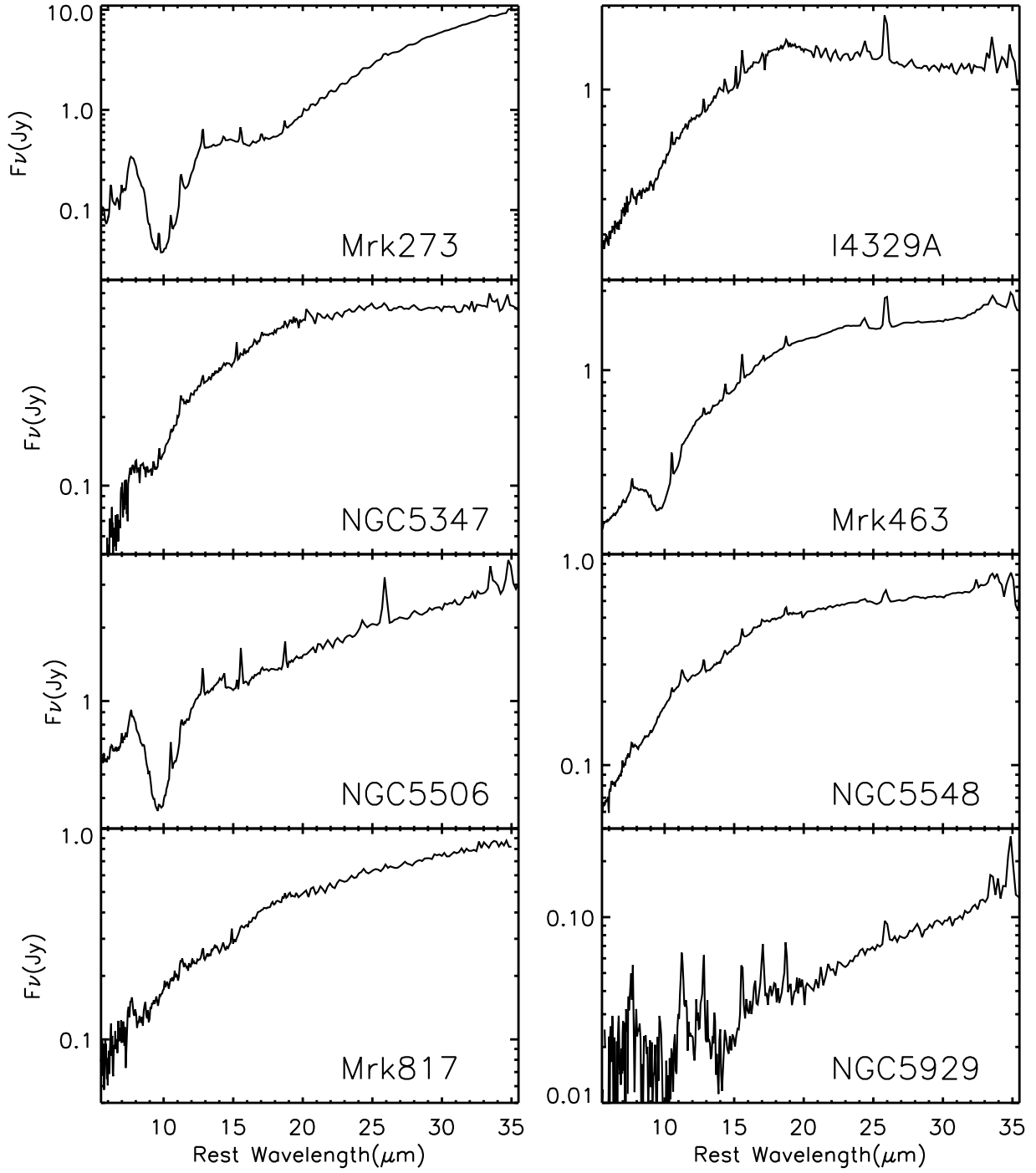


Fig. 18.— Continued.

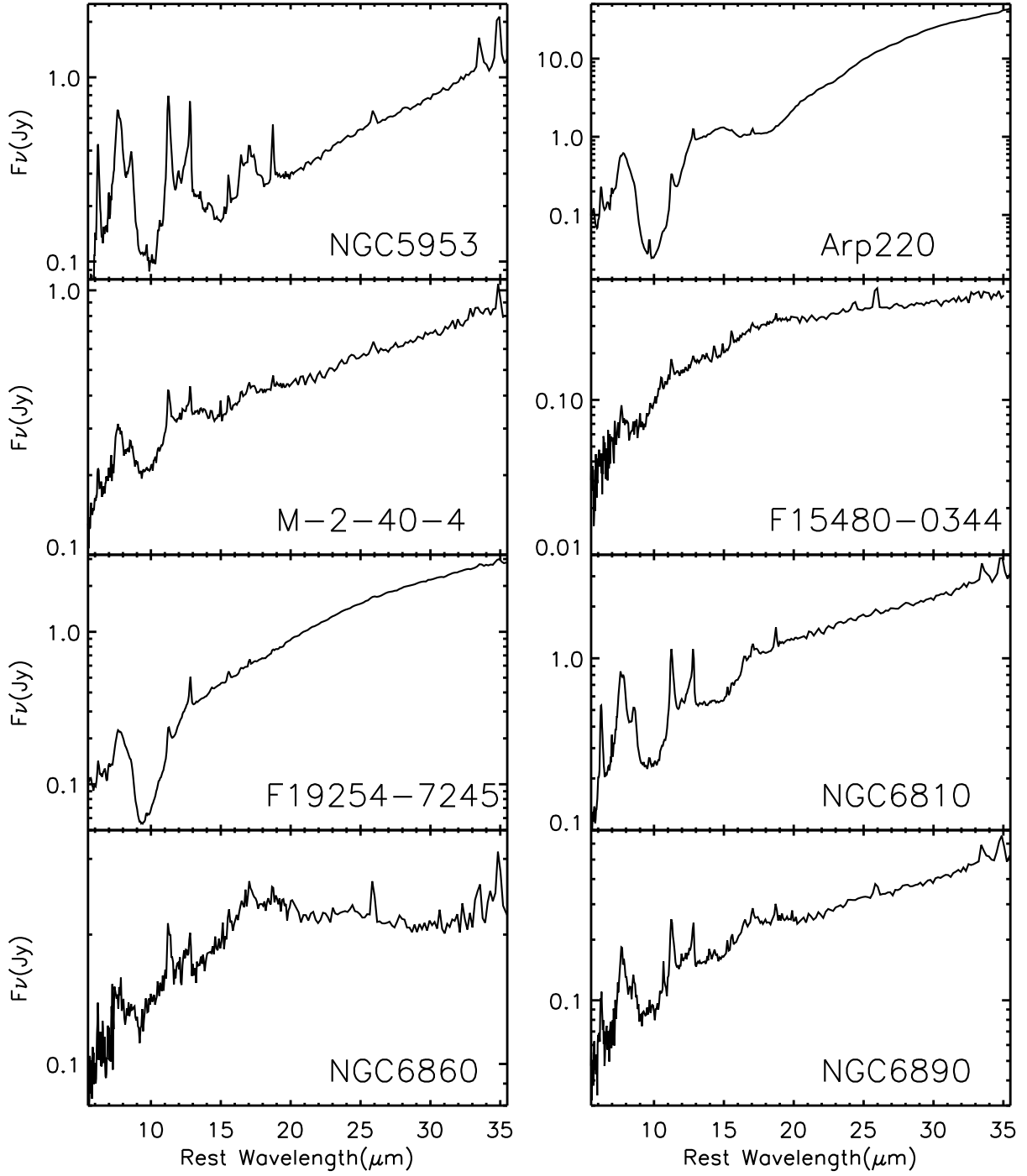


Fig. 18.— Continued.

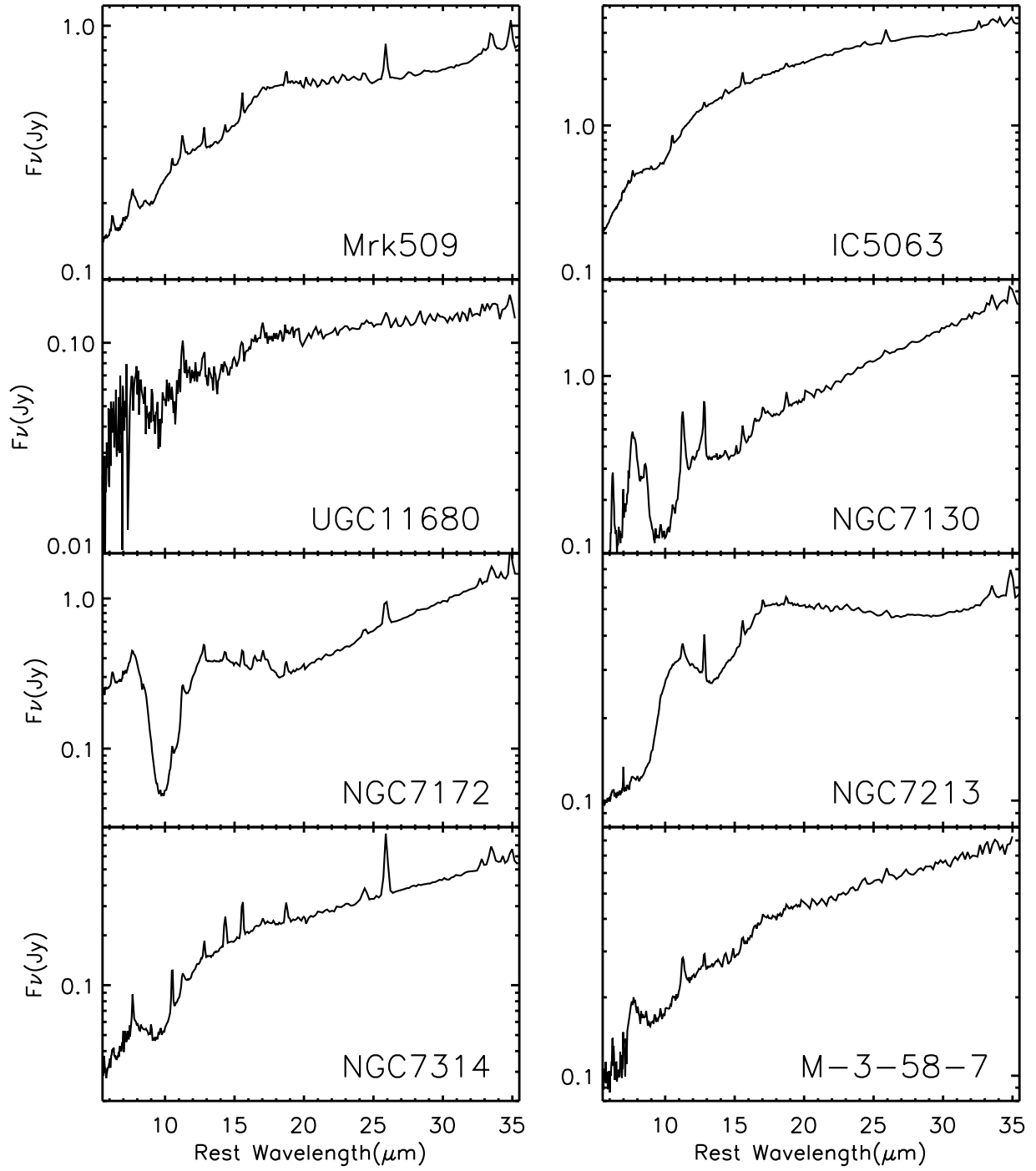


Fig. 18.— Continued.

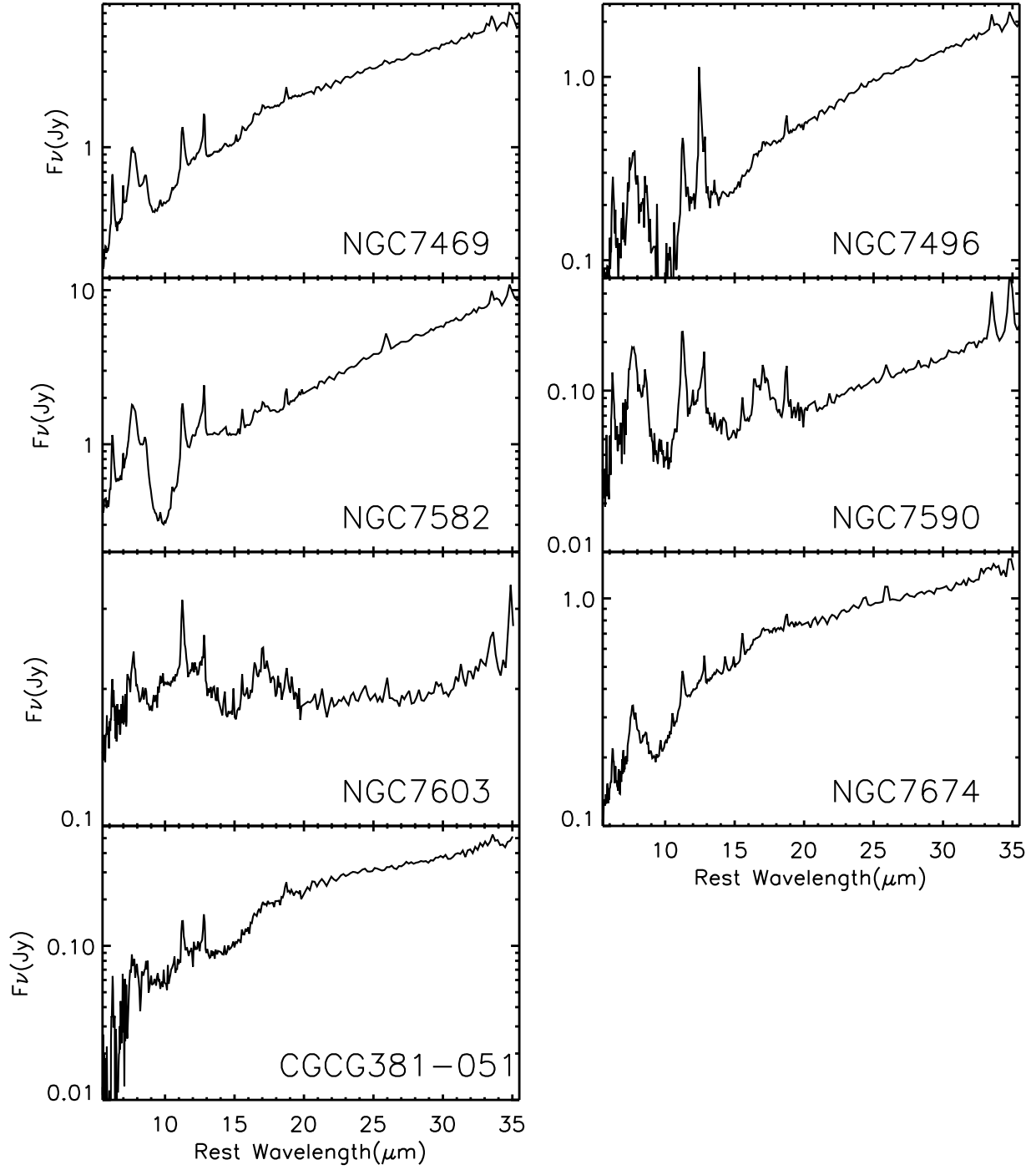


Fig. 18.— Continued.

Table 1. Properties of the Sample

Object Name	RA J2000	Dec J2000	IRAS Flux (Jy) ^a				log(L _{IR}) (L _⊙)	redshift	Type	PID
			12 μm	25 μm	60 μm	100 μm				
Mrk335	00h06m19.5s	+20d12m10s	0.27	0.45	0.35	0.57	10.72	0.026	Sy 1 ^b	3269
Mrk938	00h11m06.5s	-12d06m26s	0.35	2.39	17.05	16.86	11.48	0.020	Sy 2	3269
E12-G21	00h40m46.1s	-79d14m24s	0.22	0.19	1.51	3.22	11.03	0.030	Sy 1	3269
Mrk348	00h48m47.1s	+31d57m25s	0.49	1.02	1.43	1.43	10.62	0.015	Sy 2 ^b	3269
IZw1	00h53m34.9s	+12d41m36s	0.47	1.17	2.24	2.87	11.95	0.061	Sy 1	14
NGC424	01h11m27.6s	-38d05m00s	1.22	1.76	2.00	1.74	10.67	0.012	Sy 2 ^b	3269
NGC526A	01h23m54.4s	-35d03m56s	0.23	0.48	2.31	4.08	10.78	0.019	Sy 1 ^b	30572
NGC513	01h24m26.8s	+33d47m58s	0.25	0.48	0.41	1.32	10.52	0.020	Sy 2	3269
F01475-0740	01h50m02.7s	-07d25m48s	0.32	0.84	1.10	1.05	10.62	0.018	Sy 2	3269
NGC931	02h28m14.5s	+31d18m42s	0.62	1.42	2.80	5.66	10.92	0.017	Sy 1	3269
NGC1056	02h42m48.3s	+28d34m27s	0.34	0.48	5.33	10.20	9.93	0.005	Sy 2	3269
NGC1097	02h46m19.0s	-30d16m30s	2.96	7.30	53.35	104.79	10.78	0.004	Sy 2	159
NGC1125	02h51m40.3s	-16d39m04s	0.32	1.00	3.71	4.04	10.46	0.011	Sy 2	3269
NGC1143/4	02h55m12.2s	-00d11m01s	0.26	0.62	5.35	11.60	10.46	0.029	Sy 2	3269 ^c
M-2-8-39	03h00m30.6s	-11d24m57s	0.35	0.46	0.54	0.85	10.95	0.029	Sy 2 ^b	3269
NGC1194	03h03m49.1s	-01d06m13s	0.28	0.85	0.92	0.71	10.34	0.014	Sy 2	3269
NGC1241	03h11m14.6s	-08d55m20s	0.33	0.60	4.37	10.74	10.75	0.014	Sy 2	3269
NGC1320	03h24m48.7s	-03d02m32s	0.33	1.32	2.21	2.82	10.21	0.009	Sy 2	3269
NGC1365	03h33m36.4s	-36d08m25s	5.12	14.28	94.31	165.67	11.23	0.005	Sy 1	3269
NGC1386	03h36m46.2s	-35d59m57s	0.52	1.46	5.92	9.55	9.53	0.003	Sy 2	3269
F03450+0055	03h47m40.2s	+01d05m14s	0.29	0.39	0.87	3.92	11.10	0.031	Sy 1 ^b	3269
NGC1566	04h20m00.4s	-54d56m16s	1.91	3.02	22.53	58.05	10.61	0.005	Sy 1	159
3C120	04h33m11.1s	+05d21m16s	0.43	0.67	1.55	4.82	11.33	0.033	Sy 1	86
F04385-0828	04h40m54.9s	-08d22m22s	0.59	1.70	2.91	3.55	10.82	0.015	Sy 2	3269
NGC1667	04h48m37.1s	-06d19m12s	0.63	0.71	6.27	14.92	11.02	0.015	Sy 2	3269
E33-G2	04h55m58.9s	-75d32m28s	0.24	0.47	0.82	1.84	10.52	0.018	Sy 2 ^b	3269
M-5-13-17	05h19m35.8s	-32d39m28s	0.23	0.57	1.28	2.34	10.28	0.012	Sy 1	3269
F05189-2524	05h21m01.5s	-25d21m45s	0.74	3.47	13.25	11.84	12.17	0.043	Sy 2	86
Mrk6	06h52m12.2s	+74d25m37s	0.26	0.73	1.25	0.90	10.63	0.019	Sy 1 ^b	3269
Mrk9	07h36m57.0s	+58d46m13s	0.23	0.39	0.76	0.98	11.15	0.040	Sy 1	3269
Mrk79	07h42m32.8s	+49d48m35s	0.36	0.73	1.55	2.35	10.90	0.022	Sy 1	3269
F07599+6508	08h04m33.1s	+64d59m49s	0.33	0.54	1.75	1.47	12.57	0.148	Sy 1	105
NGC2639	08h43m38.1s	+50d12m20s	0.24	0.27	2.03	7.18	10.34	0.011	Sy 1	3269
F08572+3915	09h00m25.4s	+39d03m54s	0.33	1.76	7.30	4.77	12.15	0.058	Sy 2	105
Mrk704	09h18m26.0s	+16d18m19s	0.42	0.60	0.36	0.45	10.97	0.029	Sy 1 ^b	704
UGC5101	09h35m51.6s	+61d21m11s	0.25	1.02	11.68	19.91	12.00	0.039	Sy 1	105
NGC2992	09h45m42.0s	-14d19m35s	0.63	1.38	7.51	17.22	10.51	0.008	Sy 1	3269
Mrk1239	03h10m53.7s	-02d33m11s	0.76	1.21	1.68	2.42	11.32	0.029	Sy 1 ^b	3269
NGC3031	09h55m33.2s	+69d03m55s	5.86	5.42	44.73	174.02	9.70	0.001	Sy 1	159
3C234	10h01m49.5s	+28d47m09s	0.22	0.35	0.24	0.34	12.42	0.185	Sy 1 ^b	3624
NGC3079	10h01m57.8s	+55d40m47s	2.54	3.61	50.67	104.69	10.62	0.004	Sy 2	3269
NGC3227	10h23m30.6s	+19d51m54s	0.94	1.83	8.42	17.30	9.97	0.004	Sy 1	96
NGC3511	11h03m23.8s	-23d05m12s	1.03	0.83	8.98	21.87	9.95	0.004	Sy 1	3269
NGC3516	11h06m47.5s	+72d34m07s	0.39	0.96	2.09	2.73	10.17	0.009	Sy 1	3269

Table 1—Continued

Object Name	RA J2000	Dec J2000	IRAS Flux (Jy) ^a				log(L _{IR}) (L _⊙)	redshift	Type	PID
			12 μm	25 μm	60 μm	100 μm				
M+0-29-23	11h21m12.2s	-02d59m03s	0.48	0.76	5.85	9.18	11.36	0.025	Sy 2	3269
NGC3660	11h23m32.3s	-08d39m31s	0.42	0.64	2.03	4.47	10.47	0.012	Sy 2	3269
NGC3982	11h56m28.1s	+55d07m31s	0.47	0.97	7.18	16.24	9.81	0.004	Sy 2	3269
NGC4051	12h03m09.6s	+44d31m53s	1.35	2.20	10.53	24.93	9.66	0.002	Sy 1	3269
UGC7064	12h04m43.3s	+31d10m38s	0.22	0.88	3.48	6.25	11.18	0.025	Sy 1	3269
NGC4151	12h10m32.6s	+39d24m21s	2.01	4.87	6.46	8.88	9.95	0.003	Sy 1 ^b	14
Mrk766	12h18m26.5s	+29d48m46s	0.35	1.47	3.89	4.20	10.67	0.013	Sy 1	3269
NGC4388	12h25m46.7s	+12d39m44s	1.01	3.57	10.27	14.22	10.73	0.008	Sy 2	3269
3C273	12h29m06.7s	+02d03m09s	0.82	1.43	2.09	2.53	12.93	0.158	Sy 1 ^b	105
NGC4501	12h31m59.2s	+14d25m14s	2.29	2.98	19.68	62.97	10.98	0.008	Sy 2	3269
NGC4579	12h37m43.5s	+11d49m05s	1.12	0.78	5.93	21.39	10.17	0.005	Sy 1	159
NGC4593	12h39m39.4s	-05d20m39s	0.47	0.96	3.43	6.26	10.35	0.009	Sy 1	3269
NGC4594	12h39m59.4s	-11d37m23s	0.74	0.50	4.26	22.86	9.75	0.003	Sy 1	159
NGC4602	12h40m36.8s	-05d07m59s	0.58	0.65	4.75	13.30	10.44	0.008	Sy 1	3269
Tol1238-364	12h40m52.8s	-36d45m21s	0.72	2.54	8.90	13.79	10.87	0.011	Sy 2	3269
M-2-33-34	12h52m12.4s	-13d24m53s	0.36	0.65	1.23	2.36	10.49	0.015	Sy 1	3269
Mrk231	12h56m14.2s	+56d52m25s	1.83	8.84	30.80	29.74	12.54	0.042	Sy 1	105
NGC4922	13h01m24.9s	+29d18m40s	0.27	1.48	6.21	7.33	11.31	0.024	Sy 2	3237 ^c
NGC4941	13h04m13.1s	-05d33m06s	0.39	0.46	1.87	4.79	9.39	0.004	Sy 2	30572
NGC4968	13h07m06.0s	-23d40m37s	0.62	1.16	2.48	3.39	10.39	0.010	Sy 2	3269
NGC5005	13h10m56.2s	+37d03m33s	1.65	2.26	22.18	63.40	10.20	0.003	Sy 2	3269
NGC5033	13h13m27.5s	+36d35m38s	1.77	2.14	16.20	50.23	10.05	0.003	Sy 1	159
M-3-34-63	13h22m19.0s	-16d42m30s	0.95	2.88	6.22	6.37	11.38	0.021	Sy 2	3269
NGC5135	13h25m44.0s	-29d50m01s	0.63	2.38	16.86	30.97	11.27	0.014	Sy 2	3269
NGC5194	13h29m52.7s	+47d11m43s	7.21	9.56	97.42	221.21	10.18	0.002	Sy 2	159
M-6-30-15	13h35m53.8s	-34d17m44s	0.33	0.97	1.39	2.26	9.98	0.008	Sy 1 ^b	3269
F13349+2438	13h37m18.7s	+24d23m03s	0.61	0.72	0.85	0.90	12.32	0.108	Sy 1 ^b	61
NGC5256	13h38m17.5s	+48d16m37s	0.32	1.07	7.25	10.11	11.51	0.028	Sy 2	3269
Mrk273	13h44m42.1s	+55d53m13s	0.24	2.36	22.51	22.53	12.17	0.038	Sy 2	105
I4329A	13h49m19.2s	-30d18m34s	1.11	2.26	2.15	2.31	10.97	0.016	Sy 1 ^b	3269
NGC5347	13h53m17.8s	+33d29m27s	0.30	1.22	1.43	3.33	10.04	0.008	Sy 2	3269
Mrk463	13h56m02.9s	+18d22m19s	0.47	1.49	2.21	1.87	11.78	0.050	Sy 2	105
NGC5506	14h13m14.8s	-03d12m27s	1.29	4.17	8.42	8.87	10.44	0.006	Sy 2	3269
NGC5548	14h17m59.5s	+25d08m12s	0.43	0.81	1.07	2.07	10.66	0.017	Sy 1	30572
Mrk817	14h36m22.1s	+58d47m39s	0.38	1.42	2.33	2.35	11.35	0.031	Sy 1	3269
NGC5929	15h26m06.1s	+41d40m14s	0.43	1.67	9.52	13.84	10.58	0.008	Sy 2	3269
NGC5953	15h34m32.4s	+15d11m38s	0.82	1.58	11.79	19.89	10.49	0.007	Sy 2	3269
Arp220	15h34m57.1s	+23d30m11s	0.61	8.00	104.09	115.29	12.18	0.018	Sy 2	105
M-2-40-4	15h48m24.9s	-13d45m28s	0.41	1.45	4.09	7.06	11.32	0.025	Sy 2	3269
F15480-0344	15h50m41.5s	-03d53m18s	0.24	0.72	1.09	4.05	11.14	0.030	Sy 2	3269
F19254-7245	19h31m21.4s	-72d39m18s	0.26	1.35	5.24	8.03	12.14	0.062	Sy 2	105
NGC6810	19h43m34.4s	-58d39m21s	1.27	3.55	18.20	32.60	10.74	0.007	Sy 2	3269
NGC6860	20h08m46.9s	-61d06m01s	0.25	0.31	0.96	2.19	10.35	0.015	Sy 1 ^b	3269
NGC6890	20h18m18.1s	-44d48m25s	0.36	0.80	4.01	8.26	10.27	0.008	Sy 2	3269

Table 1—Continued

Object Name	RA J2000	Dec J2000	IRAS Flux (Jy) ^a				log(L _{IR}) (L _⊙)	redshift	Type	PID
			12 μm	25 μm	60 μm	100 μm				
Mrk509	20h44m09.7s	-10d43m25s	0.30	0.73	1.39	1.36	11.21	0.034	Sy 1	86
I5063	20h52m02.3s	-57d04m08s	1.11	3.94	5.87	4.25	10.87	0.011	Sy 2	30572
UGC11680	21h07m43.6s	+03d52m30s	0.37	0.86	2.97	5.59	11.23	0.026	Sy 2	3269
NGC7130	21h48m19.5s	-34d57m05s	0.58	2.16	16.71	25.89	11.38	0.016	Sy 2	3269
NGC7172	22h02m01.9s	-31d52m11s	0.42	0.88	5.76	12.42	10.47	0.009	Sy 2	30572
NGC7213	22h09m16.2s	-47d10m00s	0.65	0.81	2.70	8.99	10.01	0.006	Sy 1 ^b	86
NGC7314	22h35m46.2s	-26d03m01s	0.55	0.96	5.24	16.57	10.00	0.005	Sy 1	30572
M-3-58-7	22h49m37.1s	-19d16m26s	0.25	0.98	2.60	3.62	11.30	0.031	Sy 2	3269
NGC7469	23h03m15.6s	+08d52m26s	1.59	5.96	27.33	35.16	11.65	0.016	Sy 1	3269
NGC7496	23h09m47.3s	-43d25m41s	0.58	1.93	10.14	16.57	10.28	0.006	Sy 2	3269
NGC7582	23h18m23.5s	-42d22m14s	2.30	7.39	52.20	82.86	10.91	0.005	Sy 2	3269
NGC7590	23h18m54.8s	-42d14m21s	0.69	0.89	7.69	20.79	10.19	0.005	Sy 2	3269
NGC7603	23h18m56.6s	+00d14m38s	0.40	0.24	1.25	2.00	11.05	0.030	Sy 1 ^b	3269
NGC7674	23h27m56.7s	+08d46m45s	0.68	1.92	5.36	8.33	11.57	0.029	Sy 2	3269
CGCG381-051	23h48m41.7s	+02d14m23s	0.51	0.18	1.75	2.76	11.19	0.031	Sy 2	3269

^aThe IRAS fluxes are adopted from Rush et al. (1993) and Sanders et al. (2003). The uncertainties in the flux measurements range from a few percent to over 20%, averaging $\sim 10\%$.

^bWe call these sources “20 μm peakers”, which have $F_{20}/F_{30} \geq 0.95$.

^cSL only.

Table 2. PAH and Silicate Strength of the 12 μ m Seyfert Sample

Object Name	EW(6.2 μ m) (μ m)	F(6.2 μ m) ($\times 10^{-20}$ W cm $^{-2}$)	EW(11.2 μ m) (μ m)	F(11.2 μ m) ($\times 10^{-20}$ W cm $^{-2}$)	Silicate Strength ^a	Aperture Size ($''$)	Projected Size (kpc)
Mrk335	<0.074	<5.17	<0.039	<1.33	0.157	20.4 \times 15.3	11.3 \times 8.4
Mrk938	0.440 \pm 0.018	33.5 \pm 0.9	0.690 \pm 0.042	22.1 \pm 0.7	-0.991	20.4 \times 15.3	8.6 \times 6.5
E12-G21	0.278 \pm 0.017	10.9 \pm 0.3	0.325 \pm 0.005	7.53 \pm 0.03	-0.022	20.4 \times 15.3	13.0 \times 9.8
Mrk348	<0.083	<5.78	0.058 \pm 0.013	2.32 \pm 0.50	-0.333	20.4 \times 15.3	6.4 \times 4.8
IZw1	<0.018	<2.90	0.018 \pm 0.002	2.10 \pm 0.27	0.284	10.2 ^b	13.6
NGC424	<0.024	<6.95	0.010 \pm 0.001	1.53 \pm 0.09	-0.111	20.4 \times 15.3	5.1 \times 3.9
NGC526A	<0.240	<1.60	<0.012	<0.62	0.033	10.2 ^b	4.1
NGC513	0.334 \pm 0.107	9.50 \pm 1.5	0.474 \pm 0.033	9.35 \pm 0.37	0.149	20.4 \times 15.3	8.6 \times 6.5
F01475-0740	<0.177	<4.74	0.081 \pm 0.009	2.75 \pm 0.22	0.188	20.4 \times 15.3	7.7 \times 5.8
NGC931	<0.060	<7.47	0.065 \pm 0.002	4.53 \pm 0.20	-0.026	20.4 \times 15.3	7.3 \times 5.5
NGC1056	0.486 \pm 0.125	26.9 \pm 3.6	0.803 \pm 0.039	22.4 \pm 0.5	0.084	20.4 \times 15.3	2.1 \times 1.6
NGC1097	0.327 \pm 0.003	103 \pm 3	0.657 \pm 0.001	116 \pm 1	0.099	50 \times 33	4.2 \times 2.8
NGC1125	0.258 \pm 0.049	7.75 \pm 1.17	0.426 \pm 0.025	7.16 \pm 0.15	-1.022	20.4 \times 15.3	4.7 \times 3.5
NGC1143/4	0.343 \pm 0.067	18.2 \pm 1.5	0.574 \pm 0.028	13.0 \pm 0.3	... ^c	19.8 \times 16.2	12.2 \times 10.0
M-2-8-39	<0.128	<2.98	<0.047	<1.19	-0.076	20.4 \times 15.3	12.6 \times 9.4
NGC1194	<0.059	<5.05	<0.077	<2.47	-0.978	20.4 \times 15.3	6.0 \times 4.5
NGC1241	0.461 \pm 0.024	8.13 \pm 0.34	0.501 \pm 0.026	5.01 \pm 0.01	-0.908	20.4 \times 15.3	6.0 \times 4.5
NGC1320	0.082 \pm 0.019	6.86 \pm 1.24	0.074 \pm 0.003	4.60 \pm 0.11	-0.065	20.4 \times 15.3	3.8 \times 2.9
NGC1365	0.368 \pm 0.003	173 \pm 1	0.432 \pm 0.015	120 \pm 3	-0.229	20.4 \times 15.3	2.1 \times 1.6
NGC1386	0.053 \pm 0.022	5.89 \pm 1.81	0.133 \pm 0.002	9.13 \pm 0.07	-0.542	20.4 \times 15.3	1.3 \times 1.0
F03450+0055	<0.103	<6.58	<0.038	<1.62	0.027	20.4 \times 15.3	13.5 \times 10.1
NGC1566	0.223 \pm 0.034	27.6 \pm 2.8	0.470 \pm 0.004	32.2 \pm 0.4	0.105	50 \times 33	5.2 \times 3.4
3C120	<0.015	<1.35	0.014 \pm 0.002	0.904 \pm 0.142	0.130	10.2 ^b	7.2
F04385-0828	<0.058	<8.03	0.036 \pm 0.011	2.16 \pm 0.62	-0.766	20.4 \times 15.3	6.4 \times 4.8
NGC1667	0.391 \pm 0.073	17.3 \pm 1.5	0.731 \pm 0.091	15.6 \pm 1.0	-0.050	20.4 \times 15.3	6.4 \times 4.8
E33-G2	<0.102	<6.25	<0.076	<2.70	-0.247	20.4 \times 15.3	7.7 \times 5.8
M-5-13-17	0.200 \pm 0.004	6.65 \pm 0.06	0.193 \pm 0.047	5.22 \pm 0.92	-0.206	20.4 \times 15.3	5.1 \times 3.9
F05189-2524	0.037 \pm 0.001	6.54 \pm 0.16	0.062 \pm 0.003	8.02 \pm 0.35	-0.315	10.2 ^b	9.3
Mrk6	<0.097	<6.32	0.044 \pm 0.001	1.59 \pm 0.03	-0.036	20.4 \times 15.3	8.2 \times 6.1
Mrk9	<0.142	<8.12	0.116 \pm 0.030	3.54 \pm 0.82	0.050	20.4 \times 15.3	17.5 \times 13.1
Mrk79	<0.039	<4.05	0.043 \pm 0.011	2.22 \pm 0.54	-0.079	20.4 \times 15.3	9.5 \times 7.1
F07599+6508	0.027 \pm 0.001	3.36 \pm 0.14	0.018 \pm 0.001	0.97 \pm 0.06	0.113	10.2 ^b	35.0
NGC2639	<0.207	<5.40	0.530 \pm 0.036	4.70 \pm 0.19	-0.127	20.4 \times 15.3	4.7 \times 3.5
F08572+3915	<0.021	<5.25	<0.099	<2.36	-3.509	10.2 ^b	12.9
Mrk704	<0.071	<7.38	<0.029	<1.58	-0.075	20.4 \times 15.3	12.6 \times 9.4
UGC5101	0.229 \pm 0.004	12.3 \pm 0.2	0.423 \pm 0.007	10.1 \pm 0.1	-1.619	10.2 ^b	8.6
NGC2992	0.151 \pm 0.006	15.3 \pm 0.2	0.237 \pm 0.014	15.8 \pm 0.6	-0.200	20.4 \times 15.3	3.4 \times 2.6
Mrk1239	<0.029	<7.18	0.027 \pm 0.001	3.19 \pm 0.20	0.010	20.4 \times 15.3	12.6 \times 9.4
NGC3031	<0.034	<16.8	0.183 \pm 0.002	23.2 \pm 0.2	-0.035	50 \times 33	1.0 \times 0.7
3C234	<0.019	<0.82	<0.013	<0.45	-0.007	10.2 ^b	44.6
NGC3079	0.458 \pm 0.006	111 \pm 2	0.818 \pm 0.050	62.6 \pm 2.0	-0.828	20.4 \times 15.3	1.7 \times 1.3
NGC3227	0.138 \pm 0.003	24.0 \pm 0.5	0.249 \pm 0.007	29.0 \pm 0.6	-0.234	10.2 ^b	0.8
NGC3511	0.638 \pm 0.168	18.0 \pm 1.5	0.764 \pm 0.046	12.7 \pm 0.4	0.009	20.4 \times 15.3	1.7 \times 1.3
NGC3516	<0.061	<6.57	0.024 \pm 0.004	1.22 \pm 0.24	-0.158	20.4 \times 15.3	3.8 \times 2.9

Table 2—Continued

Object Name	EW(6.2 μm) (μm)	F(6.2 μm) ($\times 10^{-20} \text{ W cm}^{-2}$)	EW(11.2 μm) (μm)	F(11.2 μm) ($\times 10^{-20} \text{ W cm}^{-2}$)	Silicate Strength ^a	Aperture Size ($''$)	Projected Size (kpc)
M+0-29-23	0.437±0.099	21.0±2.5	0.619±0.082	16.7±1.1	-0.507	20.4×15.3	10.8×8.1
NGC3660	<0.434	<5.10	0.539±0.100	2.97±0.34	-0.020	20.4×15.3	5.1×3.9
NGC3982	0.467±0.058	14.4±1.1	0.787±0.049	14.0±0.3	0.110	20.4×15.3	1.7×1.3
NGC4051	0.079±0.015	9.20±1.20	0.114±0.002	9.99±0.13	0.065	20.4×15.3	0.8×0.6
UGC7064	0.364±0.015	7.90±0.21	0.527±0.055	7.87±0.43	-0.031	20.4×15.3	10.8×8.1
NGC4151	<0.011	<6.98	0.011±0.002	4.82±0.91	0.030	10.2 ^b	0.7
Mrk766	0.036±0.013	3.08±1.06	0.073±0.023	4.38±1.21	-0.274	20.4×15.3	5.6×4.2
NGC4388	0.128±0.013	15.0±1.2	0.203±0.046	14.3±2.5	-0.699	20.4×15.3	3.4×2.6
3C273	<0.013	<2.17	<0.014	<1.03	0.064	10.2 ^b	37.6
NGC4501	<0.187	<6.96	0.629±0.051	6.91±0.26	-0.232	20.4×15.3	3.4×2.6
NGC4579	0.152±0.039	14.4±2.6	0.262±0.054	8.86±1.43	0.218	50×33	5.3×3.5
NGC4593	0.044±0.005	4.82±0.57	0.089±0.014	6.10±0.85	0.063	20.4×15.3	3.8×2.9
NGC4594	0.052±0.002	13.1±0.5	0.161±0.024	7.56±0.97	-0.036	50×33	3.6×2.3
NGC4602	0.326±0.194	4.61±1.54	0.598±0.038	5.21±0.17	-0.010	20.4×15.3	3.4×2.6
Tol1238-364	0.185±0.003	15.1±0.2	0.194±0.005	14.6±0.3	-0.312	20.4×15.3	4.7×3.5
M-2-33-34	<0.304	<5.11	0.205±0.016	3.01±0.17	-0.209	20.4×15.3	6.4×4.8
Mrk231	0.011±0.001	7.50±0.39	0.028±0.001	8.77±0.35	-0.640	10.2 ^b	9.2
NGC4922	0.152±0.008	7.22±0.35	0.122±0.006	5.82±0.29	... ^c	10.2	5.1
NGC4941	<0.041	<1.06	0.038±0.016	0.82±0.34	-0.084	10.2 ^b	0.8
NGC4968	0.172±0.010	9.11±0.44	0.127±0.003	6.56±0.13	-0.206	20.4×15.3	4.3×3.2
NGC5005	0.192±0.015	18.2±1.3	0.735±0.018	28.8±0.1	-0.425	20.4×15.3	1.3×1.0
NGC5033	0.319±0.060	76.8±8.8	0.764±0.065	84.4±3.3	-0.116	50×33	3.1×2.1
M-3-34-63	0.915±0.325	4.27±0.61	1.128±0.215	3.24±0.23	0.090	20.4×15.3	9.1×6.8
NGC5135	0.384±0.032	41.6±1.9	0.594±0.039	39.2±1.3	-0.367	20.4×15.3	6.0×4.5
NGC5194	0.372±0.014	111±3	0.686±0.010	118±1	0.109	50×33	2.1×1.4
M-6-30-15	<0.063	<6.33	0.052±0.007	3.01±0.40	-0.108	20.4×15.3	3.4×2.6
F13349+2438	<0.008	<2.06	<0.013	<1.69	0.038	10.2 ^b	24.7
NGC5256	0.608±0.045	19.9±0.9	0.545±0.068	10.8±0.9	-0.692	20.4×15.3	12.1×9.1
Mrk273	0.192±0.003	13.0±0.2	0.335±0.006	8.35±0.12	-1.746	10.2 ^b	8.2
I4329A	<0.020	<6.20	<0.016	<2.85	-0.077	20.4×15.3	6.9×5.1
NGC5347	<0.112	<4.37	0.068±0.003	3.29±0.15	-0.251	20.4×15.3	3.4×2.6
Mrk463	<0.008	<1.79	0.024±0.002	2.78±0.22	-0.464	10.2 ^b	11.1
NGC5506	0.023±0.001	10.8±0.3	0.060±0.004	9.80±0.67	-0.852	20.4×15.3	2.6×1.9
NGC5548	0.018±0.005	1.08±0.32	0.047±0.007	2.71±0.38	0.040	10.2 ^b	3.7
Mrk817	<0.109	<7.60	<0.035	<1.72	-0.032	20.4×15.3	13.5×10.1
NGC5929	<0.480	<4.44	0.775±0.087	3.50±0.22	0.245	20.4×15.3	3.4×2.6
NGC5953	0.684±0.039	52.9±1.4	0.877±0.050	40.7±0.1	-0.068	20.4×15.3	3.0×2.2
Arp220	0.344±0.006	22.2±0.3	0.552±0.023	15.4±0.6	-2.543	10.2 ^b	3.9
M-2-40-4	0.066±0.002	8.25±0.17	0.119±0.004	8.29±0.21	-0.068	20.4×15.3	10.8×8.1
F15480-0344	<0.190	<5.29	0.075±0.016	2.45±0.48	-0.159	20.4×15.3	13.0×9.8
F19254-7245	0.064±0.002	5.09±0.18	0.134±0.006	5.06±0.22	-1.345	10.2 ^b	13.7
NGC6810	0.419±0.020	56.1±1.4	0.463±0.002	46.4±0.3	-0.158	20.4×15.3	3.0×2.2
NGC6860	0.084±0.018	6.32±1.28	0.095±0.008	3.59±0.28	0.005	20.4×15.3	6.4×4.8
NGC6890	0.237±0.020	9.66±0.57	0.277±0.028	8.33±0.58	-0.054	20.4×15.3	3.4×2.6

Table 2—Continued

Object Name	EW(6.2 μm) (μm)	F(6.2 μm) ($\times 10^{-20} \text{ W cm}^{-2}$)	EW(11.2 μm) (μm)	F(11.2 μm) ($\times 10^{-20} \text{ W cm}^{-2}$)	Silicate Strength ^a	Aperture Size ($''$)	Projected Size (kpc)
Mrk509	0.042 \pm 0.002	4.92 \pm 0.19	0.068 \pm 0.002	4.77 \pm 0.16	-0.002	10.2 ^b	7.5
I5063	0.011 \pm 0.002	2.14 \pm 0.34	0.019 \pm 0.002	3.96 \pm 0.40	-0.263	10.2 ^b	2.4
UGC11680	<0.334	<7.77	0.166 \pm 0.019	2.50 \pm 0.25	0.142	20.4 \times 15.3	11.3 \times 8.4
NGC7130	0.493 \pm 0.044	32.7 \pm 1.9	0.430 \pm 0.001	25.2 \pm 0.1	-0.227	20.4 \times 15.3	6.9 \times 5.2
NGC7172	0.045 \pm 0.001	9.25 \pm 0.29	0.204 \pm 0.009	7.52 \pm 0.05	-1.795	10.2 ^b	1.9
NGC7213	0.022 \pm 0.002	1.73 \pm 0.20	0.037 \pm 0.007	2.88 \pm 0.51	0.236	10.2 ^b	1.2
NGC7314	0.063 \pm 0.007	1.63 \pm 0.18	0.087 \pm 0.013	1.87 \pm 0.27	-0.476	10.2 ^b	1.0
M-3-58-7	0.074 \pm 0.002	5.58 \pm 0.13	0.099 \pm 0.024	5.03 \pm 1.10	-0.047	20.4 \times 15.3	13.5 \times 10.1
NGC7469	0.293 \pm 0.003	60.8 \pm 0.5	0.288 \pm 0.012	45.4 \pm 1.2	-0.159	20.4 \times 15.3	6.9 \times 5.2
NGC7496	0.912 \pm 0.189	44.6 \pm 4.5	0.590 \pm 0.002	21.6 \pm 0.1	-0.626	20.4 \times 15.3	2.6 \times 1.9
NGC7582	0.274 \pm 0.023	101 \pm 5	0.457 \pm 0.006	77.1 \pm 0.3	-0.833	20.4 \times 15.3	2.2 \times 1.6
NGC7590	0.496 \pm 0.005	14.0 \pm 0.1	0.854 \pm 0.082	13.0 \pm 0.5	0.023	20.4 \times 15.3	2.2 \times 1.6
NGC7603	0.056 \pm 0.004	7.08 \pm 0.53	0.121 \pm 0.006	6.22 \pm 0.24	0.211	20.4 \times 15.3	13.0 \times 9.8
NGC7674	0.132 \pm 0.006	14.2 \pm 0.4	0.129 \pm 0.013	10.0 \pm 0.8	-0.215	20.4 \times 15.3	12.6 \times 9.4
CGCG381-051	0.542 \pm 0.031	5.07 \pm 0.16	0.211 \pm 0.037	4.04 \pm 0.47	0.316	20.4 \times 15.3	13.5 \times 10.1

^aThe error in the silicate measurement is determined by the S/N of the continuum flux, which has an absolute uncertainty of $\sim 5\%$.

^bSpectrum extracted from IRS staring mode. The size of the LL slit is 2 pixel wide, where 1 pixel $\sim 5.1''$.

^cTo measure the silicate feature, a complete 5-35 μm spectrum is needed. This source only has an SL spectrum from 5-14.5 μm .

Table 3. 11.2 μm PAH EWs for the 12 μm Seyfert sample

	Seyfert 1		Seyfert 2	
	EW(μm)	Sources	EW(μm)	Sources
Whole sample ^a	0.154 \pm 0.216	47	0.352 \pm 0.312	56
Whole sample ^b	0.205 \pm 0.215	37	0.384 \pm 0.299	52
L _{IR} < 10 ¹¹ L _⊙ ^a	0.171 \pm 0.235	29	0.356 \pm 0.318	35
L _{IR} ≥ 10 ¹¹ L _⊙ ^a	0.127 \pm 0.184	18	0.345 \pm 0.310	21
L _{IR} < 10 ¹¹ L _⊙ ^b	0.217 \pm 0.232	24	0.395 \pm 0.303	32
L _{IR} ≥ 10 ¹¹ L _⊙ ^b	0.185 \pm 0.188	13	0.367 \pm 0.300	20
F25/F60 > 0.2 ^a	0.068 \pm 0.116	33	0.143 \pm 0.237	30
F25/F60 ≤ 0.2 ^a	0.358 \pm 0.262	14	0.592 \pm 0.191	26
F25/F60 > 0.2 ^b	0.102 \pm 0.119	24	0.177 \pm 0.237	26
F25/F60 ≤ 0.2 ^b	0.397 \pm 0.227	13	0.592 \pm 0.191	26

^aValues calculated including the upper limits on PAH EWs.

^bValues calculated excluding the upper limits on PAH EWs.